Pergamon

Geochimica et Cosmochimica Acta, Vol. 68, No. 11, pp. 2543–2560, 2004

0016-7037/04 $30.00 + .00

doi:10.1016/j.gca.2003.10.017

U-Th-Pb and $^{230}Th/^{238}U$ disequilibrium isotope systematics: Precise accessory mineral chronology and melt evolution tracing in the Alpine Bergell intrusion

FELIX OBERLI,[1,*] MARTIN MEIER,[1] ALFONS BERGER,[2] CLAUDIO L. ROSENBERG,[3] and RETO GIERÉ[4]

[1]Institut für Isotopengeologie und Mineralische Rohstoffe, ETH-Zentrum, CH-8092 Zürich, Switzerland
[2]Mineralogisch-Petrographisches Institut, Universität Bern, CH-3012 Bern, Switzerland
[3]Fachbereich Geowissenschaften, Freie Universität Berlin, D-12249 Berlin, Germany
[4]Earth and Atmospheric Sciences, Purdue University, West Lafayette, IN 47907-2051, USA

(*Received October* 12, 2001; *accepted in revised form October* 15, 2003)

Abstract—In order to investigate the potential of combined Th-U-Pb isotope and $^{230}Th/^{238}U$ disequilibrium systematics for tracing magmatic crystallization and melt evolution, conventional high-resolution single-crystal TIMS techniques have been applied to zircon, titanite and fragments of geochemically characterized growth zones of allanite. These minerals were extracted from a single tonalite specimen collected from the feeder zone of the Tertiary Bergell pluton (Southern Steep Belt, S Switzerland/N Italy). The isotopic results document an extended history of crystallization and melt evolution of at least 5 Ma, with well-resolved zircon ages defining an early interval of 33.0 to 32.0 Ma, followed by crystallization of zoned allanite from 32.0 to 28.0 Ma and formation of magmatic epidote possibly as late as 26 Ma. Trace and major element patterns in zoned allanite closely mirror melt evolution, characterized by increase of U concentration and sharp decrease of Th and LREE, reflecting early crystallization of phases low in U and, in particular, the dominating control by allanite precipitation.

Preservation of substantial quantities of excess ^{206}Pb derived from initial excess ^{230}Th in all analyzed allanite grains indicates that their isotopic systems have not been reset by loss of radiogenic Pb during prolonged residence at magmatic conditions and regional-metamorphic cooling, and that the measured sequence of $^{208}Pb/^{232}Th$ dates translates into a real age sequence. Major loss of radiogenic Pb from compositionally zoned allanite by volume diffusion would have resulted in a data pattern grossly different from the observed one, as demonstrated by numerical modeling of ^{232}Th-^{208}Pb-^{238}U-^{230}Th-^{206}Pb isotopic evolution. The results therefore suggest closure temperatures $\geq$700°C for magmatic allanite.

Quantification of $^{230}Th/^{238}U$ disequilibrium relationships reveals a smooth, initially steep decrease of Th/U in the magma from values of 2.9 at 32.0 Ma to $<$ 0.1 at 28.0 Ma in equilibrium with sequential allanite zoning. Comparison of calculated $(Th/U)_{magma}$ with measured total-rock Th/U = 0.79 requires fractional crystallization of allanite at an early stage. This process of removal of allanite, and thus Th, from the melt was operative at least until ~31.5 Ma, providing an upper limit for the time of emplacement of the studied magma batch. The fact that bulk zircon and a large part of allanite crystallization predate emplacement cautions against equating ages determined on refractory minerals from deep-seated plutons with intrusion ages.

The persistence of magmatic conditions over a period of ~5 Ma, concentrated in a narrow collision zone between the European and the African plate, has been a major controlling factor for the Oligocene evolution of the adjacent Insubric fault, the main tectonic lineament of the Alps being active from late Cretaceous to Miocene times.

1. INTRODUCTION

Accessory minerals are the predominant hosts of U, Th and rare earth elements (REE) in intermediate and acid igneous rocks and thus provide a record of trace element evolution during magma generation and differentiation processes. Some of the accessories are rather refractory and serve as robust isotopic geochronometers, zircon and monazite being the most prominent examples. The main focus of the present study is directed to allanite, an accessory mineral of great promise for quantification of igneous processes. Its relatively large size (compared to zircon or monazite) in combination with an often well developed zonation pattern and high contents of REE and actinides makes allanite a suitable candidate for detailed investigation of trace element evolution vs. time, given that crystallization has lasted long enough to be resolved by isotopic dating techniques and that the bulk of in situ produced radiogenic daughter element is retained at magmatic crystallization temperatures.

In contrast to the predominant practice of dating accessory minerals exclusively by the U-Pb method, the present study makes full use of both U-Pb *and* Th-Pb isotope systematics. When dating minerals characterized by high Th/U (e.g., allanite), special attention, however, has to be paid to the fact that the observed (apparent) $^{206}Pb/^{238}U$ ages can be considerably enhanced by excess ^{206}Pb derived from ^{230}Th, an intermediate daughter nuclide of the ^{238}U decay series incorporated in excess of its secular equilibrium ratio. High-resolution $^{206}Pb/^{238}U$ data, in particular those measured on relatively young samples, therefore require correction for radioactive disequilibrium (see Schärer, 1984). Such corrections are commonly based on the assumption that Th/U of the melt from which the minerals grew can be approximated by Th/U measured in their

* Author to whom correspondence should be addressed (oberli@erdw.ethz.ch).

host rock. Implicitly, it is also assumed that the crystallizing melt has remained close to radioactive equilibrium. As will be demonstrated by this study, these assumptions do not necessarily hold for natural crystallization environments, because fractional crystallization of Th- or U-enriched phases can result in considerable divergence between Th/U in a crystallizing melt and its solidified total-rock products (e.g., Amelin and Zaitsev, 2002). If fractionation occurs at time scales similar to or shorter than the half-life of ^{230}Th (75.38 ka), such a process will also cause ^{230}Th/^{238}U in the residual melt to deviate from secular equilibrium.

In view of all these difficulties, ^{235}U-^{207}Pb dating would be a viable alternative to the use of the ^{238}U-^{206}Pb system, provided that there is no gross initial enrichment in intermediate daughter nuclide ^{231}Pa ($T_{1/2}$ = 32.76 ka) relative to its primary parent ^{235}U, a condition, which is not always fulfilled (Mortensen et al., 1997; Anczkiewicz et al., 2001). The presence of even a moderate common Pb component in young allanite, however, results in imprecise ^{235}U-^{207}Pb ages. Th-Pb dating is not affected by these problems, because there are no long-lived intermediate daughter nuclides in the ^{232}Th-^{208}Pb decay system, and the effect of common Pb is mitigated by relatively high Th concentrations (e.g., Barth et al., 1989). Therefore, Th-Pb clearly is the method of choice for precise and accurate dating of allanite or other Th enriched minerals (Barth et al., 1994). In this context it is rather astonishing, that recent applications of this technique, with rare exceptions (e.g., Amelin and Zaitsev, 2002), are mostly confined to measurements by ion microprobe (e.g., Catlos et al., 2000).

Rather than "discarding" the information on initial radioactive disequilibrium available from the ^{238}U-^{206}Pb system by uncertain corrections, the present study intends to make full use of it. We will show that quantitative evaluation of the relationship between disequilibrium-affected ^{238}U-^{206}Pb ages and "unbiased" ^{232}Th-^{208}Pb ages has a considerable potential for obtaining detailed information on the nature of geological processes dated by the latter. Of particular importance is the fact that preservation of an initial disequilibrium signature can be indicative of a primary crystallization age as opposed to the resetting of a mineral age by reheating beyond closure temperature during a metamorphic event (Copeland et al., 1988) or exposure to prolonged postmagmatic cooling (von Blanckenburg, 1992).

In this paper we report results obtained by high-precision U-Th-Pb measurements on single-crystals and fragments of zircon, allanite and titanite, prepared from a single tonalite sample of the Tertiary Bergell pluton. By correlation of major and trace element measurements with Th-Pb ages and U-Th-Pb isotope systematics determined on fragments of distinct domains from zoned allanite we will establish and date a process of sequential compositional evolution of allanite and melt controlled by fractional crystallization. The combined results will lead us to the conclusion that the accessory mineral population of the investigated rock has conserved a record of magmatic activity covering an extensive time interval of ≥5 Ma, with all analyzed zircon and a substantial part of allanite clearly predating the emplacement of the magma batch sampled for this study.

2. GEOLOGICAL SETTING AND SAMPLE DESCRIPTION

The Oligocene calc-alkaline Bergell pluton (Fig. 1) is located in the Eastern Central Alps and intrudes the Penninic nappes north of the Insubric fault, which represents the W segment of the Periadriatic fault system (Berger et al., 1996; Trommsdorff and Nievergelt, 1983). The Insubric fault, the major tectonic lineament in the Central Alps (e.g., Schmid et al., 1989), separates the Penninic and Austroalpine nappes, which underwent Tertiary greenschist- to granulite-facies metamorphism, from the Southern Alps, which were almost unaffected by thermal events during Tertiary times.

The geometry of the pluton is essentially conformable to the Penninic nappe system, which forms a steep belt (Southern Steep Belt) near the Insubric fault and changes into a subhorizontal stack-pile of recumbent folds north of the pluton. The subvertical tonalitic segment of the intrusion adjacent to the Insubric fault represents the feeder zone for the main tonalitic-granodioritic body of the pluton, which develops into a ballooning structure further north. Reusser (1987) and Davidson et al.(1996) showed that pressures recorded by magmatic amphibole gradually increase from east to west, an effect that can be explained by postmagmatic tilting on an N-S trending axis (Villa and von Blanckenburg, 1991; Rosenberg and Heller, 1997). Consequently, the present-day erosion surface exposes successively deeper levels of the intrusion, from the shallow roof of the main mass in the east to the deep-seated feeder zone exposed as a tail-shaped extension in the west. Isotope-geochemical arguments suggest that the Bergell pluton and similar contemporaneous I-type granitoid intrusions along the Periadriatic fault system are mainly derived by extensive melting of lower crustal sources, with some contributions from an enriched lithospheric mantle and upper crust (von Blanckenburg et al., 1992, 1998). An overview of the regional geology of the Bergell area is given by Gieré and Stahel (1996).

For the present study, we have used a sample from the westernmost part of the tonalite tail (Fig. 1; Swiss grid coordinates 727.2/115.3). Hornblende barometry (≈0.8 GPa) suggests an intrusion depth in excess of 20 km for this part of the pluton (Davidson et al., 1996; Reusser, 1987). The country rocks in this area experienced regional high-grade metamorphism (Todd and Engi, 1997) at the time of emplacement, as documented by their high-grade foliations, which are parallel to the magmatic foliation of the pluton (Berger et al., 1996; Hafner, 1993). The tonalite mainly consists of plagioclase, biotite, hornblende and quartz, and contains allanite, epidote, titanite, zircon and magnetite as accessory minerals. It displays a well-developed magmatic foliation and lineation by parallel alignment of larger crystals of hornblende and plagioclase (Berger et al., 1996). Magmatic epidote commonly occurs as a rim around allanite. To avoid overprint by postintrusive metamorphic events, the tonalite specimen was collected from the northern edge of the tonalite tail, which is devoid of metamorphic reactions of the type amphibole + anorthite ± orthoclase → epidote + biotite + albite that affected the southern part of the tonalite tail (Berger and Stuenitz, 1996). The chosen rock sample was closely examined from a microstructural point of view and was characterized in detail both petrographically and chemically. Bulk composition and modal abundance are given in Table 1.

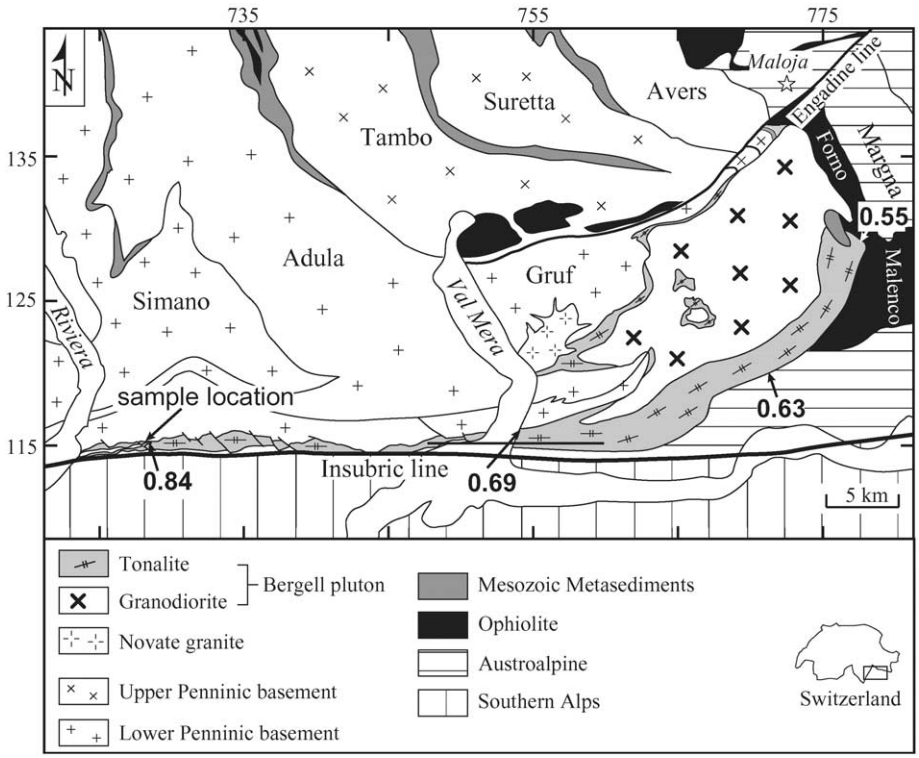

Fig. 1. Geological map of Bergell pluton intruding Penninic and Austroalpine basement and cover nappes just north of the Insubric fault, straddling the border between SE Switzerland and N Italy. Numbers with arrows represent hornblende equilibration pressures in GPa, which increase from E to W along the pluton.

3. PREVIOUS AGE DETERMINATIONS

For a detailed compilation and interpretation of geochronological data for the Bergell intrusion and its regional environment the reader is referred to Hansmann (1996), whereas summaries of the Alpine and pre-Alpine evolution of the Central Alps can be found in Gebauer (1999) and Schaltegger and Gebauer (1999). For brevity, only a few selected studies are mentioned here. Using Pb-α counting techniques, Grünenfelder and Stern (1960) were able to assign a Tertiary age of 25 to 30 $\pm$ 10 Ma to the Bergell intrusion. Gulson and Krogh (1973) then estimated an age of ~30.3 Ma based on U-Pb isotope data for multi-grain fractions of zircon containing inherited components as well as other accessory minerals from various lithologies of the pluton.

Table 1. Whole-rock major and trace element composition by XRF and TIMS, and modal composition.

	wt.%		ppm		vol.%[a]
SiO_2	59.9	Ba	270	Plagioclase	55.7
Al_2O_3	18.0	Ce	70	Biotite	12.9
Fe_2O_3[b]	5.97	Cr	10	Quartz	11.6
MnO	0.112	Nd	13.5[c]	Hornblende	14.1
MgO	3.1	Ni	10	Epidote	4.8
CaO	6.36	Pb	9.18[c]	Allanite	0.88
Na_2O	3.0	Rb	73.6[c]	Opaques	0.05
K_2O	1.74	Sm	4.03[c]		
P_2O_5	0.14	Sr	281[c]		
LoI[d]	0.65	Th	4.47[c]		
Sum	99.52	U	5.62[c]		
		V	190		
		Y	30		
		Zn	40		
		Zr	140		

[a] Based on 4500 thin-section point counts.
[b] Total Fe; $Fe^{3+}/(Fe^{2+} + Fe^{3+}) = 0.30$.
[c] Isotope dilution data by TIMS.
[d] Loss on ignition; $H_2O^- = 0.18$, $H_2O^+ = 0.92$ wt.%.

Modern high-resolution U-Th-Pb ages finally became available when von Blanckenburg (1992) reported precise zircon, allanite and titanite ages of 31.88 $\pm$ 0.09 Ma for tonalite and a younger age of 30.13 $\pm$ 0.17 Ma for granodiorite from the eastern shallower part of the pluton. Villa and von Blanckenburg (1991) showed that $^{40}Ar/^{39}Ar$ ages and K-Ar ages along an E-W traverse of the intrusion decrease from 28.59 $\pm$ 0.16 Ma (hornblende) and 26.4 $\pm$ 0.6 Ma (biotite) in the east to ~24.8 $\pm$ 1.4 and 21.0 $\pm$ 0.6 Ma in the western, more deeply eroded part of the intrusion, a consequence of later eastward tilting of the Alpine block on a N-S trending axis, and cooling in a temperature field inherited from high-grade regional metamorphism that affected the southern Central Alpine region. Biotite K-Ar ages measured on tonalitic boulders from "molasse" deposits in the southern Alpine foreland (Como-Varese region, N Italy) (Giger and Hurford, 1989; Giger, 1991) also support a long lasting cooling history. Boulders from the base of the stratigraphic column displaying massive magmatic texture yielded K-Ar ages of ~32.9 to 30.7 Ma, whereas boulders at higher stratigraphic levels characterized by ductile deforma-

tion were derived from deeper parts of the pluton and had younger ages of ~29.8 to 26.9 Ma (analytical errors amounting to ±0.3–0.5 Ma).

4. ANALYTICAL PROCEDURES

4.1. U-Th-Pb

After reduction of the sample to <300-μm particle size, heavy-mineral concentrates enriched in zircon, allanite-epidote and titanite were obtained by Wilfley table, standard heavy-liquid separation techniques and a Frantz Isodynamic Magnetic Separator. Part of the allanite-epidote concentrate was further divided into four distinct density fractions (3.30–3.64, 3.64–3.73, 3.73–3.90, and 3.90–4.05 g cm^{-3}) using Clerici's solution diluted with distilled H_2O. To remove potential impurities and alteration effects from the outer parts of the crystals and their fragments, most of the samples were air abraded (Krogh, 1982) in an Al_2O_3 dish. Before abrasion, the zircon crystals were carefully inspected for potential presence of older inherited components. The grains were mounted in glycerol and studied by transmitted light microscopy for detection of three-dimensional interior surfaces outlined by minuscule fluid inclusions and other impurities that can be indicative of overgrown cores. Similar means were used for elimination of allanite and titanite fragments containing zircon inclusions or showing intergrowth.

U-Pb analysis in zircon followed the procedure described by Meier and Oberli in Wiedenbeck et al. (1995). Allanite and titanite samples were cleaned in p.a. grade organic solvents (acetone, hexane, ethanol) and H_2O in an ultrasonic bath, spiked with a mixed ^{233}U-^{235}U-^{230}Th-^{205}Pb tracer and decomposed in Krogh type PTFE dissolution vessels (Krogh, 1973) in a 1:1 mixture of concentrated HF and HCl. Pb, U and Th were extracted by standard HBr, HCl and HNO_3 anion-resin exchange techniques (details are available from the first author on request). Isotopic measurements were performed on a Varian MAT Tandem single-collector mass spectrometer, using a Faraday collector or a highly linear secondary-electron multiplier in low-gain analog mode, and filament-loading procedures as described in Wiedenbeck et al. (1995). For details on blank and data reduction parameters the reader is referred to the caption of Table 2.

4.2. Electron Microprobe

Quantitative chemical analyses of allanite were performed at the Institut für Mineralogie und Petrographie, ETH Zürich using a Cameca SX-50 electron microprobe equipped with five wavelength-dispersive spectrometers and operated at 15 kV with a beam current of 20 nA measured on a Faraday cage. Natural and synthetic minerals, and synthetic oxides and glasses were used as standards. Data collection time was 20 s for most major elements and 100 s for REE, Th and U. Data collection on background positions above and below the peaks was half the time of data collection on respective peak position. The raw data were corrected on-line with a PAP correction procedure (Pouchou and Pichoir, 1984). The method used for REE analysis and correction of interelement interferences followed guidelines by Williams (1996).

5. RESULTS

5.1. Zircon

The U-Pb isotope results obtained on seven air abraded single zircon crystals are presented in Tables 2 and 3 and in Figure 2. Six of the grains (z1–z6), selected to be free of inherited cores, form a narrow cluster on Concordia curve at 32 to 33 Ma. Grain z7, which exhibited interior features strongly suggestive of an older core, plots at a distinctly discordant position corresponding to an apparent $^{206}Pb/^{238}U$ age of 45 Ma. Because of young age and modest U concentration (108–228 ppm), analytical errors in $^{207}Pb/^{235}U$ are considerably larger than those in $^{206}Pb/^{238}U$. Further discussion of the results is therefore exclusively based on the latter, more precise values.

The $^{206}Pb/^{238}U$ ratios of the data plotted in Figure 2 are corrected for initial disequilibrium (depletion) of ^{238}U-derived ^{230}Th, adopting Th/U = 3.0 for the host melt. This correction increases the $^{206}Pb/^{238}U$ ages by ~90 ka (Table 3). Given the information on the evolution of Th/U in the melt vs. time, which will become available from the interpretation of the allanite data in section 6.4, the uncertainty of this correction is probably <20 ka. This is insignificant in comparison to analytical errors of 0.10 to 0.27 Ma estimated for the $^{206}Pb/^{238}U$ ages.

The $^{206}Pb/^{238}U$ data of z1 to z6 clustering at 32.0 to 33.0 Ma do not define a single age value at the 95% confidence level. Analyses z1 and z5, for example are clearly resolved from each other. Possible explanations for the limited, but significant spread of the data are (1) presence of tiny inherited cores not detected by prior microscopic inspection, (2) postcrystallization loss of radiogenic Pb, and (3) crystallization over an extended time interval. Based on the data pattern displayed in Figure 2, none of these hypotheses can be rejected a priori, and complementary information is needed to assess their relative importance.

A plot of U concentration vs. $^{206}Pb/^{238}U$ age (Fig. 3) displays a regular increase of U concentration with time, ranging from 108 ppm at 33.0 Ma (z1) to ~150 ppm at 32.2 to 32.0 Ma (z5 and z6). The arrow labeled "Inheritance" points in the direction of zircon z7 located far off the diagram at an age of 44.8 Ma and a U concentration of 228 ppm. Variable contributions by similar inherited components to zircon crystallizing at 33 to 32 Ma thus would result in a mixing trend which is distinct from that exhibited by zircons forming part of the cluster. The data are thus at variance with hypothesis 1.

The distinction of postcrystallization loss of radiogenic Pb (hypothesis 2) from an extended crystallization scenario (hypothesis 3) is more problematic. In both cases, abrasion of outer crystal portions for elimination of surface-correlated alteration can enhance the apparent age of the grain. Zircons z1, z2 and z3, which occupy the older segment of the data trend, have been reduced to 59, 55 and 54% of their original width, respectively (width before abrasion = 200, 210 and 180 μm), whereas samples z4, z5 and z6 were abraded less severely (to 89, 80 and 97% of their original width of 140, 240 and 140 μm). From this information it is evident that the data distribution shown in Figure 3 is controlled to some degree by abrasion. The tight correlation of U concentration with age, however, suggests an extended period of crystallization of growth-

Table 2. U-Th-Pb TIMS results.

Sample[a]	Weight[b] (μg)	U (ppm)	Th (ppm)	Th/U (wt)	Pb_{rad}[c] (ppm)	Pb_{com}[d] (ppm)	Pb_{com}[e] (pg)	$^{206}Pb/^{204}Pb$[f]	$^{207}Pb/^{235}U$[g]	$^{206}Pb/^{238}U$[g]	ρ[h]	$^{208}Pb/^{232}Th$[g]
z1 (1) abr	6.1	108	—	0.38[i]	0.56	0.49	4.6	63.09	0.0314 ± 31	0.005112 ± 24	–0.034	—
z2 (1) abr	4.9	126	—	0.52[i]	0.67	0.11	2.1	104.2	0.0319 ± 34	0.005055 ± 32	0.034	—
z3 (1) abr	4.0	128	—	0.48[i]	0.67	0.05	1.7	100.5	0.0323 ± 35	0.005056 ± 27	–0.355	—
z4 (1) abr	6.7	137	—	0.49[i]	0.71	0.08	2.1	142.7	0.0321 ± 22	0.005006 ± 42	0.051	—
z5 (1) abr	24.1	146	—	0.42[i]	0.74	0.29	8.5	146.6	0.0319 ± 14	0.004965 ± 18	0.471	—
z6 (1) abr	8.1	149	—	0.51[i]	0.78	0.24	3.5	121.7	0.0325 ± 16	0.005007 ± 15	–0.132	—
z7 (1) abr	8.3	228	—	0.36[i]	1.60	0.15	2.8	298.7	0.0526 ± 11	0.006953 ± 26	0.190	—
a1 (7) A [3.90–4.05] abr	145.5	78.0	13,440	172.3	19.5	5.79	854	23.78	0.0347 ± 84	0.005959 ± 66	0.948	0.001583 ± 8
a2 (9) A [3.73–3.90] abr	366.7	215	12,663	59.0	18.8	9.01	3315	27.11	0.0310 ± 46	0.005514 ± 37	0.935	0.001568 ± 8
a3 (10) [>3.30] abr	472.0	254	7188	28.3	11.3	8.60	4072	28.64	0.0305 ± 30	0.005250 ± 25	0.940	0.001566 ± 9
a4 (9) [>3.30] abr	337.9	378	4802	12.7	8.45	9.89	3355	31.43	0.0288 ± 24	0.005195 ± 20	0.947	0.001554 ± 11
a5 (1) B2 [3.64–3.73]	56.7	340	3674	10.8	6.61	12.36	713	28.05	0.0282 ± 36	0.005379 ± 29	0.950	0.001512 ± 13
a6 (1) B2 [3.64–3.73]	39.4	403	2136	5.30	4.66	16.33	656	26.65	0.0264 ± 43	0.005102 ± 33	0.909	0.001479 ± 24
a7 (1) B2 [3.30–3.64]	57.8	615	1444	2.35	4.54	18.38	1075	29.01	0.0278 ± 27	0.004841 ± 22	0.953	0.001450 ± 34
a8 (1) B2 [3.30–3.64]	29.2	769	917	1.19	4.53	17.34	519	32.35	0.0282 ± 23	0.004903 ± 20	0.933	0.001408 ± 51
a9 (1) B2 [3.30–3.64]	61.6	557	1140	2.05	3.80	17.25	1075	28.52	0.0270 ± 29	0.004777 ± 24	0.948	0.001385 ± 40
epl (1) D [3.30–3.64]	48.0	90.2	4.56	0.051	0.31	23.87	1158	19.71	[j]	0.00399 ± 17	0.934	—
ti1 abr[k]	682.5	764	—	0.06[i]	3.24	21.66	14798	29.25	0.0278 ± 17	0.004640 ± 17	0.822	—
ti2 abr	76.2	345	—	–0[i]	1.43	2.13	174	63.41	0.0299 ± 10	0.004644 ± 10	0.876	—
ti3 abr	48.3	288	—	0.05[i]	1.23	1.69	93.9	62.35	0.0296 ± 12	0.004633 ± 12	0.918	—

[a] z = zircon, a = allanite, ep = epidote, ti = titanite; () number of grains/fragments in analysis; A, B1, B2, D: correlation with individual zones in allanite based on Th concentration (see text); [] density fraction from which the allanite fragments were selected; abr: air abraded sample.

[b] Weighed to a precision of ±0.3 μg (2σ reproducibility) using an ultra-micro balance.

[c] Concentration of radiogenic lead in sample.

[d] Concentration of common lead in sample (corrected for analytical blank).

[e] Content of common lead in analysis (includes analytical blank).

[f] Measured ratio corrected for mass fractionation only.

[g] Radiogenic lead. Analytical uncertainties are given at the 95% confidence level and refer to the least significant digits of the corresponding values. Data corrected for mass fractionation, analytical blank and sample common lead using the parameters given below. $^{206}Pb/^{238}U$ values are not corrected for disequilibrium in initial $^{230}Th/^{238}U$.

[h] Correlation coefficient of $^{207}Pb/^{235}U$ vs. $^{206}Pb/^{238}U$.

[i] Calculated from radiogenic $^{208}Pb/^{206}Pb$ for t = 32 Ma.

[j] Value not resolved due to elevated common lead contents.

[k] Sample originating from a titanite grain extracted from a rock fragment using a dentist's drill.

Parameters used for data reduction and error propagation (reproducibility given at 1σ level):

(1) Isotope dilution by mixed ^{233}U-^{235}U-^{230}Th-^{205}Pb tracer.

(2) Mass fractionation correction factors (amu^{-}): Pb = 1.0009 ± 0.0004, U = correction by double spike techniques, Th = 1.000 ± 0.001 (relative to tracer calibration).

(3) Zircon blank data: Pb_{tot} = 1.5 ± 0.3 pg, $^{208}Pb/^{206}Pb$ = 2.086 ± 0.031, $^{207}Pb/^{206}Pb$ = 0.864 ± 0.017, $^{204}Pb/^{206}Pb$ = 0.05508 ± 0.00034, ρ(^{206}Pb vs. $^{207}Pb/^{206}Pb$) = 0.81, ρ(^{206}Pb vs. $^{204}Pb/^{206}Pb$) = 0.60, ρ($^{207}Pb/^{206}Pb$ vs. $^{204}Pb/^{206}Pb$) = 0.76. U < 1 pg.

(4) Allanite and titanite blank data: Pb_{tot} = 12.2 ± 3.1 pg, $^{208}Pb/^{206}Pb$ = 2.097 ± 0.019, $^{207}Pb/^{206}Pb$ = 0.848 ± 0.005, $^{204}Pb/^{206}Pb$ = 0.0547 ± 0.0012, ρ(^{206}Pb vs. $^{208}Pb/^{206}Pb$) = −0.01, ρ(^{206}Pb vs. $^{207}Pb/^{206}Pb$) = −0.54, ρ(^{206}Pb vs. $^{204}Pb/^{206}Pb$) = −0.999, ρ($^{208}Pb/^{206}Pb$ vs. $^{204}Pb/^{206}Pb$) = −0.04, ρ($^{207}Pb/^{206}Pb$ vs. $^{204}Pb/^{206}Pb$) = 0.57. U typically <3 pg (in one case 6.5 pg due to memory after processing a large sample). Th typically <3 pg (in one case 5.6 pg due to memory after processing a large sample). No blank corrections performed for U and Th.

(5) Initial Pb composition at 32 Ma calculated from whole-rock U-Th-Pb data (concentrations given in Table 1): $^{208}Pb/^{206}Pb$ = 2.0730 ± 0.0012, $^{207}Pb/^{206}Pb$ = 0.83630 ± 0.00024, $^{204}Pb/^{206}Pb$ = 0.053308 ± 0.000032, ρ($^{208}Pb/^{206}Pb$ vs. $^{204}Pb/^{206}Pb$) = −0.928, ρ($^{207}Pb/^{206}Pb$ vs. $^{204}Pb/^{206}Pb$) = 0.921.

Table 3. U-Th-Pb age results and melt evolution parameters.

Sample	$^{206}Pb/^{238}U$ age[a] (Ma)	$^{206}Pb/^{238}U$ age[b] (Ma)	$^{208}Pb/^{232}Th$ age (Ma)	$\Delta_{Th\text{-}U\ age}$[c] (Ma)	f[d]	Th/U magma[e]	Th/U magma[f]
z1	32.87 ± 16	32.97 ± 16					
z2	32.50 ± 21	32.59 ± 21					
z3	32.51 ± 18	32.60 ± 18					
z4	32.19 ± 27	32.28 ± 27					
z5	31.93 ± 12	32.02 ± 12					
z6	32.19 ± 10	32.28 ± 10					
z7	44.67 ± 17	44.76 ± 17					
a1	38.30 ± 42		31.97 ± 17	6.33 ± 45	59.2 ± 42	2.91 ± 41	2.91
a2	35.45 ± 24		31.66 ± 17	3.79 ± 29	35.9 ± 27	1.65 ± 25	1.25
a3	33.75 ± 16		31.64 ± 18	2.12 ± 24	20.5 ± 22	1.38 ± 30	1.05
a4	33.40 ± 13		31.38 ± 22	2.02 ± 26	19.5 ± 24	0.65 ± 16	0.49
a5	34.58 ± 19		30.54 ± 26	4.04 ± 32	38.2 ± 30	0.28 ± 4	0.27
a6	32.81 ± 22		29.87 ± 48	2.93 ± 52	27.9 ± 48	0.19 ± 7	0.18
a7	31.13 ± 14		29.29 ± 68	1.84 ± 70	18.0 ± 64	0.13 ± 9	0.12
a8	31.53 ± 13		28.44 ± 103	3.10 ± 104	29.5 ± 95	0.04 ± 3	0.04
a9	30.72 ± 15		27.98 ± 80	2.74 ± 82	26.2 ± 75	0.08 ± 5	0.07
ep1	25.7 ± 11						
ti1	29.84 ± 11						
ti2	29.87 ± 7						
ti3	29.80 ± 7						

[a] Not corrected for initial radioactive disequilibrium in $^{230}Th/^{238}U$.
[b] Corrected for initial radioactive disequilibrium adopting $(Th/U)_{magma} = 3.0$ (see text).
[c] $\Delta_{Th\text{-}U\ age} = (^{206}Pb/^{238}U)_{age} - (^{208}Pb/^{232}Th)_{age}$.
[d] Fractionation factor $f = (Th/U)_{crystal}/(Th/U)_{magma}$.
[e] $(Th/U)_{wt}$ in magma at mean time of crystallization of corresponding allanite sample calculated from f and measured Th/U in allanite; data not corrected for disequilibrium in $(^{230}Th/^{238}U)_{magma}$.
[f] Same as (e), but corrected for disequilibrium in $(^{230}Th/^{238}U)_{magma}$ (see text).
Analytical uncertainties are given at the 95% confidence level and refer to the least significant digits of the corresponding volumes.

zoned zircon in a differentiating melt rather than resetting by loss of radiogenic Pb. While resetting cannot be excluded a priori, the relatively young age of the zircons and their generally moderate U concentration make this less likely. If the latter interpretation is correct, each zircon age must then represent an integral of a finite growth period rather than marking a single short-lived growth "event." This leads to the conclusion that zircon crystallization had commenced at or before 33.0 Ma and lasted until or beyond 32.0 Ma.

5.2. Allanite

5.2.1. Mineral Chemistry of Allanite

Allanite is relatively abundant in the tonalite (~0.9 vol.%, see Table 1). All crystals are optically zoned, showing a dark brown core and a lightly colored to colorless rim. This change in optical properties is reflected by chemical composition, which changes from allanite in the center to REE-free epidote in the rim (Figs. 4 and 5). Most of the allanite crystals are elongated along the <b> direction and range in length from 3 to 5 mm. A back-scattered electron (BSE) image of part of a typical allanite grain (Fig. 4a) displays a core, which is distinctly brighter than the surrounding rim due to elevated contents of heavier elements (e.g., Th, REE). The crystal shows complex internal zoning, as documented by different shades of gray (Fig. 4b). Of particular interest is the fact that both core and rim consist of at least two individual subzones (labeled A and B, and C and D, respectively). The rim zones C and D are separated by a distinct straight boundary (dashed line in Fig. 4a), which traces an euhedral shape. This is in marked contrast to the boundary between zones A and B in the core. Figure 4b reveals that zone B can be further subdivided into at least two additional zones, B1 and B2. The complex dentate, serrate and embayed boundaries observed in the core area possibly reflect various growth and corrosion stages during allanite crystallization from a melt.

To quantify the pronounced zoning observed in the BSE images, we have performed a series of electron probe microanalyses (EPMA) along the traverse depicted in Figure 4. Table 4 lists the average compositions for the various zones identified in Figure 4. As shown in Figure 5, the core is characterized by high contents of Th + REE and is also enriched in Ti relative to the rim (Table 4). Figure 5 further shows that the calculated Fe^{3+} content of the core is significantly lower than that of the rim. We note that the interior parts of the studied crystal exhibit Fe^{3+}/Fe_{tot} values of ~0.4, whereas the rim contains essentially no Fe^{2+}. Table 4 further demonstrates that the total REE content decreases dramatically from core ($REE_2O_3 \approx 17.6$ wt.%) to rim ($REE_2O_3 \approx 0$ wt.%).

This decrease is accompanied by strong fractionation effects (Fig. 6). Zone A exhibits a chondrite-normalized pattern that is typical for many allanites (strong LREE enrichment). In comparison to zone A, the LREE enrichment is less pronounced in zone B, which is particularly evident for zone B2. The younger zone C is poor in REE and exhibits a nearly flat chondrite-normalized pattern. In zone D, the youngest part of the crystal, the REE contents are generally below electron probe detection limits and the composition corresponds to epidote. The regular, correlated changes in major and trace element compositions are distinct from those resulting from hydrothermal overprint (e.g.,

Poitrasson, 2002) and thus suggest that the observed zonation in allanite is an expression of a magmatic crystallization sequence.

5.2.2. Th-U-Pb Systematics of Allanite

The Th-U-Pb isotope results obtained on nine allanite samples are listed in Table 2, arranged according to decreasing $^{208}Pb/^{232}Th$ age (Table 3). Samples a3 and a4 consisted of 9 to 10 homogeneous, dark-brown to semiopaque fragments directly selected from the bulk allanite concentrate (density fraction >3.30). Substantial differences in the resulting U and Th concentrations (Table 2) that correlate with minor (although within-error) differences in the $^{208}Pb/^{232}Th$ and $^{206}Pb/^{238}U$ ages (Table 3) suggested that more selective preparation techniques might potentially resolve significant age differences within the population of allanite fragments and might establish a systematic relationship between age and U and Th content. We therefore divided the allanite concentrate into four density classes to obtain fractions of distinct compositional range (section 4.1). Single- as well as multiple-fragment analyses performed on these density fractions, together with analyses a3 and a4, show a very large spread in both, Th-Pb and U-Pb ages, and Th, U and common Pb concentrations (Tables 2 and 3). A comparison of Th concentrations obtained by isotope dilution analysis (TIMS data, Table 2) with the EPMA data for the allanite crystal displayed in Figure 4 (Table 4) links the isotopic results to the zoning pattern.

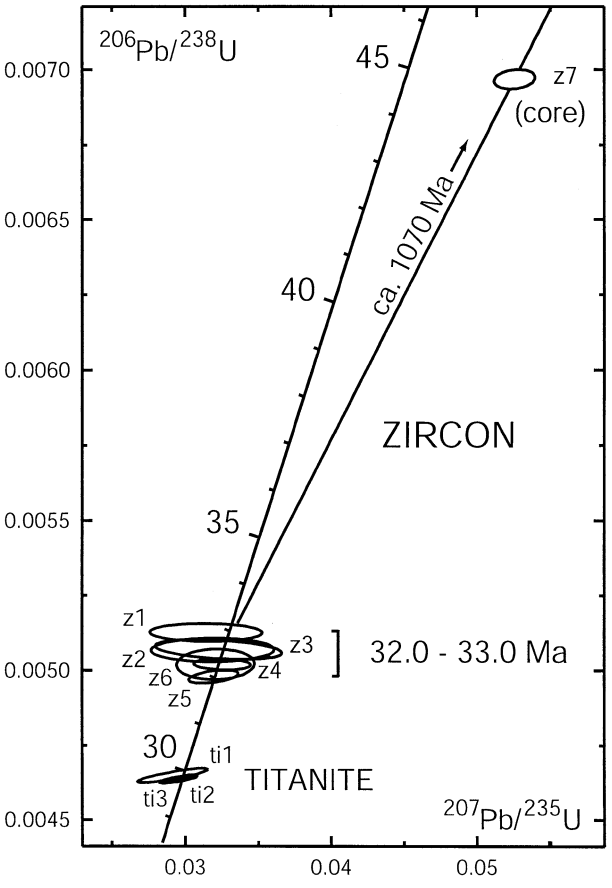

Fig. 2. Concordia representation of single-zircon U-Pb data. The $^{206}Pb/^{238}U$ values are corrected for initial radioactive disequilibrium in $^{230}Th/^{238}U$.

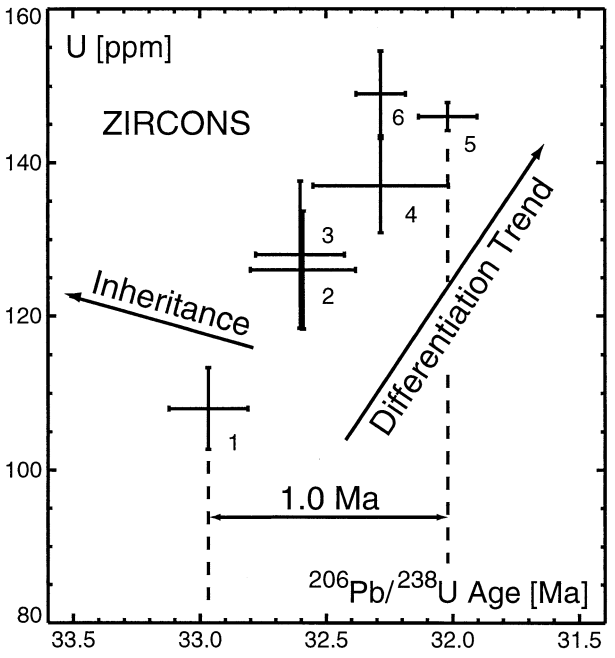

Fig. 3. Plot of U concentration vs. $^{206}Pb/^{238}U$ age for zircon analyses shown in Figure 2. The increase of U concentration with decreasing age is interpreted to reflect the increase of incompatible element concentration in a differentiating magma. The arrow labeled "inheritance" points to the position of core-bearing zircon 7, which plots far off to the left of the differentiation trend.

To avoid bias from initial radioactive disequilibrium in $^{230}Th/^{238}U$ and for better precision, we have chosen to use $^{208}Pb/^{232}Th$ ages rather than Pb/U ages for time reference. A striking feature of these Th-Pb ages is the extensive time interval of ~4 Ma populated by the results (Table 3). As expected, the $^{206}Pb/^{238}U$ ages are all distinctly and variably older than the corresponding $^{208}Pb/^{232}Th$ ages, due to substantial ^{206}Pb contribution from decay of excess initial ^{230}Th. This has important implications for the assessment of age significance and for the interpretation of the magma evolution process (sections 6.3 and 6.6).

Figures 7a to 7c reveal striking correlations between Th, U, and Pb_{com} concentrations and observed $^{208}Pb/^{232}Th$ ages. The Th concentrations decrease with time from ~1.3 wt.% in the core zone (A) at ~32 Ma (sample 1) to ~0.1 wt.% at ~28 Ma (sample 9) in the outer portion of the central area (zone B2; Fig. 7a). During the same time interval, U concentrations increase from 78 ppm to 560 to 770 ppm (Fig. 7b). Similarly, common Pb contents increase from 6 ppm to 17 to 18 ppm (Fig. 7c). The antithetical trends of Th and U concentration in allanite with time result in an enhanced trend for the Th/U ratio (Fig. 7d), which decreases sharply from a high initial value of ~170 for the oldest fragments to low values of 1 to 2 at the end of the documented path. These observations can readily be interpreted in terms of trace element evolution in a fractionating magma system. During the ~4-Ma crystallization interval documented by the Th-Pb ages, substantial amounts of Th were incorporated

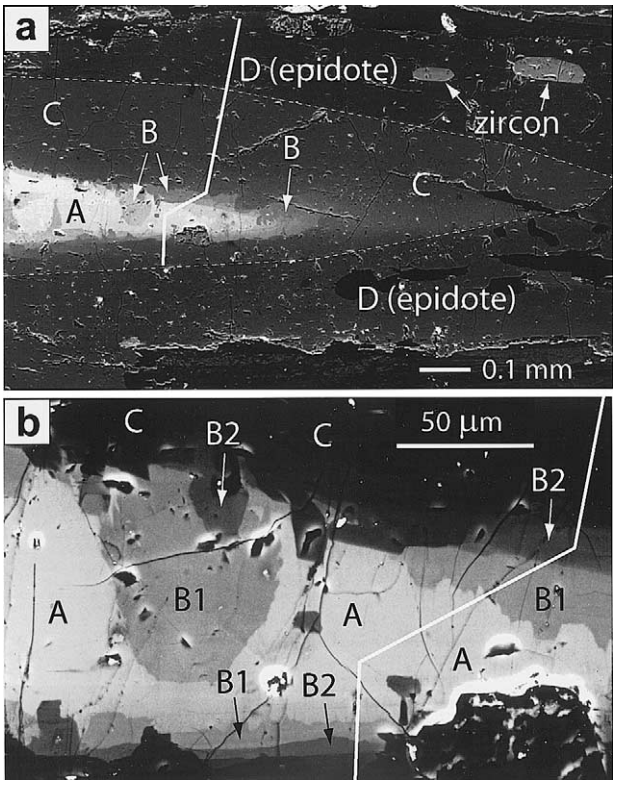

Fig. 4. BSE micrograph of part of the allanite crystal studied by electron microprobe (solid line shows trace of EPMA profile). (a) The bright core (zones A and B) displays complex zoning, which is shown in more detail in (b). The euhedral boundary between the allanite rim zone (C) and epidote (D) is marked by the dashed line.

by crystallizing allanite, causing the melt to become severely depleted in Th with time. On the other hand, crystallization of major mineral phases with low U and Pb concentrations in combination with only moderate U content in early allanite led to increasing concentrations of U and Pb in the course of magma differentiation.

5.3. Epidote

A yellowish fragment selected from the lowest density fraction of the allanite concentrate contains 90 ppm of U and 4.6 ppm of Th (Table 2). It is not clear whether the fragment originates from the epidote rim of an allanite crystal (zone D; mean U ~ 80 ppm by EPMA) or from a grain not associated with an allanite core. Because of low $^{206}Pb/^{204}Pb$ (19.7), the fragment yields a rather imprecise $^{206}Pb/^{238}U$ age of 25.7 ± 1.1 Ma (Table 3), which is younger than the youngest Th-Pb age measured for allanite (28.0 ± 0.8 Ma, a9). The contents of radiogenic ^{207}Pb and ^{208}Pb are too low to give meaningful complementary age constraints.

5.4. Titanite

Three abraded titanite grains yield a concordant cluster in Figure 2, with indistinguishable $^{206}Pb/^{238}U$ ages of 29.84 ± 0.11, 29.87 ± 0.07 and 29.80 ± 0.07 Ma (Table 3). In contrast to zircon and allanite, there is no clear-cut correlation of these ages with U concentration (290–760 ppm; Table 2). Th/U values obtained from radiogenic $^{208}Pb/^{206}Pb$ are very low (<0.1; Table 2) and are highly imprecise due to low contents of radiogenic ^{208}Pb and large corrections for common ^{208}Pb ($[^{208}Pb]_{rad}/[^{208}Pb]_{com} \approx 0.02$ for sample ti3, radiogenic component not resolved for sample ti2). Because Th-Pb ages could thus not be derived from these data, no Th measurements were performed on the titanites.

5.5. Total-Rock Rb-Sr and Sm-Nd Results

Total-rock concentrations for Rb, Sr, Sm and Nd determined by isotope dilution TIMS techniques are listed in Table 1. Present-day $^{87}Sr/^{86}Sr$ is 0.708815 ± 0.000027 (=0.70849 at 30 Ma) (adjusted to $^{87}Sr/^{86}Sr$ = 0.710240 adopted for the NIST SRM 987 Sr standard). Present-day $^{143}Nd/^{144}Nd$ is 0.512444 ± 0.000011 (adjusted to $^{143}Nd/^{144}Nd$ = 0.511927 adopted from Wasserburg et al., 1981, for the Ndβ isotopic standard), corresponding to $\varepsilon_{CHUR}(0) = -3.79$ and $\varepsilon_{CHUR}(30\ Ma) = -3.72$ (constants from Farmer and DePaolo, 1983). Errors are given at the 95% confidence level and include external variance terms for run-to-run reproducibility (Oberli et al., 1999).

6. DISCUSSION

The almost "perfect" magmatic evolution signature displayed by major and trace element patterns in allanite (Table 4, Figs. 5 and 6) and their tight correlation with sequential Th-Pb ages of individual zones suggest that these ages might be a direct expression of the time scale of magmatic evolution. Such a hypothesis, however, needs to be carefully evaluated, because the sample originates from an area where regional metamorphic peak temperatures of ~670°C may have been reached relatively late, i.e., at ~28 Ma (Engi et al., 1995), and were followed by slow cooling (Villa and von Blanckenburg, 1991). The observed age decrease from core to rim in allanite (and zircon) could thus simply reflect loss of radiogenic Pb at elevated temperatures. To distinguish between the two contrast-

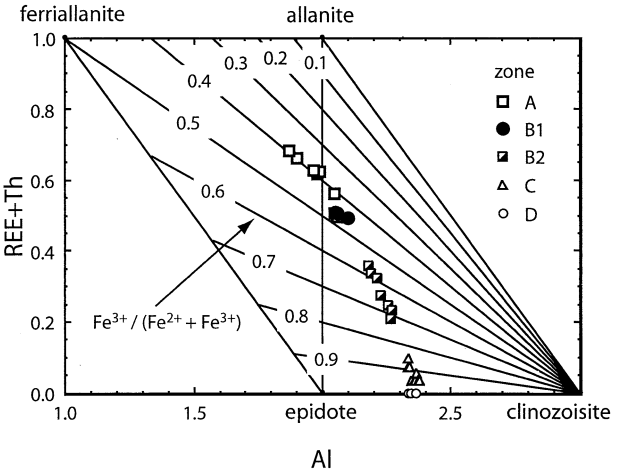

Fig. 5. Allanite substitution relations and Fe^{3+}/Fe_{tot} grid (diagram adopted from Petrik et al., 1995). See Figure 4 for the location of zones A to D.

Table 4. Major and trace element concentrations (wt.%) of individual growth zones in allanite (see Fig. 4).

Zone	A average	A std dev	B1 average	B1 std dev	B2 average	B2 std dev	C average	C std dev	D average	D std dev
MgO	1.30	0.24	1.03	0.03	0.59	0.09	0.22	0.04	0.09	0.01
Al_2O_3	18.83	0.86	20.23	0.36	22.88	0.72	25.55	0.35	26.00	0.09
SiO_2	33.32	0.38	34.48	0.16	36.27	0.59	38.25	0.42	38.77	0.31
CaO	13.69	0.92	15.12	0.21	18.42	0.88	22.28	0.50	23.57	0.09
TiO_2	0.37	0.08	0.27	0.02	0.19	0.02	0.17	0.01	0.19	0.01
MnO	0.37	0.01	0.36	0.01	0.30	0.01	0.25	0.01	0.23	0.00
FeO (tot)	11.76	0.38	11.46	0.29	10.75	0.14	10.15	0.21	10.45	0.04
La_2O_3	5.67	0.87	4.22	0.11	2.16	0.64	0.23	0.12	<0.07	
Ce_2O_3	9.46	0.93	8.16	0.19	4.74	0.96	0.76	0.36	<0.06	
Pr_2O_3	0.84	0.04	0.86	0.04	0.59	0.11	0.16	0.07	<0.13	
Nd_2O_3	1.50	0.12	1.80	0.08	1.51	0.30	0.59	0.26	<0.10	
Sm_2O_3	0.17	0.05	0.17	0.03	0.17	0.03	0.14	0.02	<0.12	
ThO_2	1.40	0.20	1.01	0.25	0.29	0.24	<0.01		<0.01	
U_2O_3	<0.01		<0.01		0.06	0.02	0.02	0.01	0.01	0.02
Subtotal	98.69		99.18		98.94		98.75		99.30	
FeO (calc)	6.98		6.45		4.22		1.44		0.41	
Fe_2O_3 (calc)	5.31		5.56		7.26		9.67		11.16	
H_2O (calc)	1.67		1.72		1.81		1.91		1.95	
Total	100.90		101.46		101.48		101.63		102.37	
Σ (REE_2O_3)	17.65		15.21		9.18		1.87			
Normalized on the basis of eight cations										
Mg	0.173		0.133		0.073		0.026		0.010	
Al	1.988		2.075		2.232		2.361		2.360	
Si	2.984		3.001		3.002		2.998		2.986	
Ca	1.314		1.409		1.634		1.871		1.945	
Ti	0.025		0.018		0.012		0.010		0.011	
Mn	0.028		0.026		0.021		0.016		0.015	
Fe (tot)	0.881		0.834		0.744		0.665		0.673	
La	0.187		0.136		0.066		0.007		0.000	
Ce	0.310		0.260		0.144		0.022		0.000	
Pr	0.027		0.027		0.018		0.004		0.000	
Nd	0.048		0.056		0.045		0.017		0.000	
Sm	0.005		0.005		0.005		0.004		0.000	
Th	0.029		0.020		0.006		0.000		0.000	
U	0.000		0.000		0.000		0.000		0.000	
OH (stoich)	1.000		1.000		1.000		1.000		1.000	
Fe^{3+} (calc)	0.358		0.364		0.452		0.570		0.647	
Fe^{2+} (calc)	0.523		0.469		0.292		0.095		0.026	
Fe^{3+}/Fe (tot)	0.407		0.437		0.608		0.858		0.961	
Σ (REE)	0.578		0.484		0.277		0.053		0.000	
REE + Th + U	0.607		0.504		0.283		0.053		0.000	
Mg + Fe^{2+}	0.696		0.603		0.365		0.120		0.037	

ing hypotheses, we will examine isotopic closure behavior, with special emphasis on Th-U-Pb isotope systematics.

6.1. Estimates of Crystallization Temperatures

Liquidus-solidus properties of tonalitic melts only provide a rough temperature frame for the investigated mineral association. Liquidus temperatures at 1.5-GPa range from 1250°C (dry melt) to 940°C (H_2O excess) (Huang and Wyllie, 1986). At the pressure of ~0.8 GPa established by hornblende barometry, the water-saturated solidus provides a minimum temperature of ~650°C (Lambert and Wyllie, 1974). Hornblendes from the western part of the pluton give temperatures of ~920 to 960°C (Reusser, 1987).

Under water-saturated conditions buffered at NNO, magmatic epidote reaches its upper thermal stability at 700°C at 0.8 GPa, and at 790°C at 1.4 GPa (Schmidt and Thompson, 1996). These values, which represent upper limits for magma temperature at the time of transition from the allanite cores to the epidote rims for pressures ≥0.8 GPa, must be considered approximate, because the magma was probably undersaturated with respect to H_2O (Reusser, 1987). Textural relationships between allanite and epidote allow an estimate of minimum crystallization temperature for allanite. Allanite in our sample is commonly overgrown by epidote, whereas the reverse is not observed. It is therefore likely that early allanite crystallized at temperatures exceeding the stability field of epidote, i.e., above 700°C.

For the measured bulk-rock Zr content of 140 ppm, a zircon saturation temperature of 727°C can be calculated from the model of Watson and Harrison (1983), if a melt composition similar to the tonalite total rock is adopted ($M = [Na + K + 2Ca]/[Al \cdot Si] = 2.08$). This, however, can result in substantial underestimation of the saturation temperature, because for the same bulk composition, a residual melt fraction in the presence of plagioclase and hornblende crystals would have

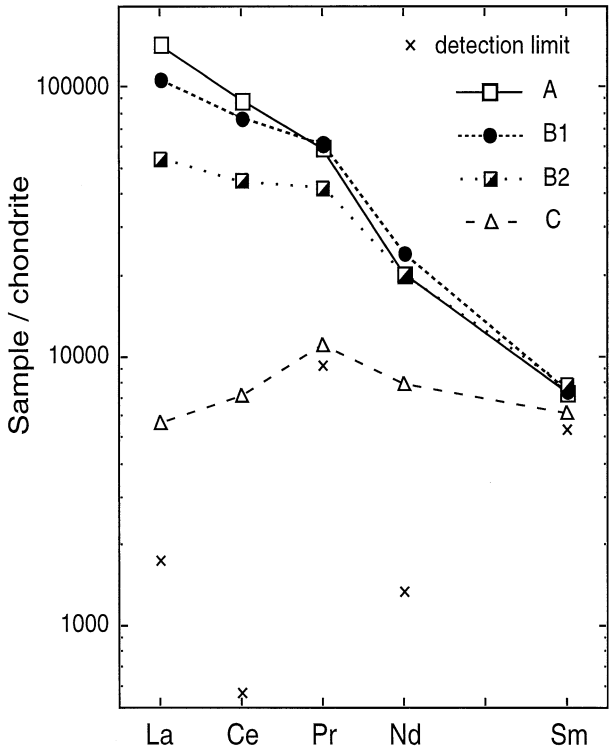

Fig. 6. Chondrite-normalized REE patterns within individual zones in allanite changing from highly LREE enriched in the core (A) to nearly flat for the rim (C). Chondrite data from Wakita et al. (1971).

lower M values and higher Zr concentrations (Hansmann and Oberli, 1991). Conversely, overestimation of dissolved Zr due to the occurrence of inherited xenocrysts (e.g., sample z7) would lead to an overestimation of the saturation temperature.

6.2. Isotopic Closure of Zircon and Allanite

The closure temperature concept (Dodson, 1973) furnishes a conventional base for assessing isotopic age significance, provided there is information on diffusion parameters and rate of temperature change. Calculations based on the diffusion constants determined by Lee et al. (1997) and Cherniak and Watson (2000) indicate that the closure temperature for 120-μm-sized non-metamict zircon grains exceeds the temperature of ~730°C estimated from zircon saturation by >100°C, even when unreasonably low cooling rates of 1°C/Ma are adopted or when the diffusion constants are expanded by their analytical error bounds. At temperatures <830°C, purely temperature-controlled diffusion loss of radiogenic Pb would therefore not appear to be a viable explanation for the observed 1-Ma spread in U-Pb ages. On the other hand, numerous studies have shown that *metamict* zircon can loose radiogenic Pb at temperatures below those prevailing during magmatic processes, in particular, when exposed to fluids (for a discussion of Pb loss mechanisms see summary by Mezger and Krogstad, 1997). Because of young age and low U content of the zircons, and because evidence of magmatic or metamorphic hydrothermal overprint of our sample is essentially lacking, low-temperature Pb loss is not a likely cause for age variation. The observed tight correlation between decreasing age and increasing U concentration as well as the close sequence of zircon and oldest allanite ages therefore favor an interpretation in terms of a primary crystallization age signature.

No diffusion data are yet available for allanite. U-Pb age data on zircon, allanite and titanite extracted from rocks associated with the metamorphic core zone of southeast British Columbia have shown the retentivity of radiogenic Pb in allanite to exceed that of titanite at upper amphibolite facies conditions (Heaman and Parrish, 1991). A closure temperature of 650 ± 25°C was derived from these observations (Heaman and Parrish, 1991; Spear and Parrish, 1996; Parrish, 2001). As will be demonstrated by the isotopic arguments following below, such a low closure temperature appears to be at variance with our results.

We conclude that the preceding arguments do not offer a reliable handle for an accurate assessment of the significance of the zircon and allanite age results. For allanite, however, it will be shown that quantitative evaluation by means of Th-U-Pb isotope systematics can considerably reduce ambiguity in data interpretation.

6.3. Preservation or Absence of a "Fossil" Initial Radioactive Disequilibrium Signature in Allanite: Crystallization vs. Closure Ages

The allanites carry a significant ^{206}Pb excess component, which is expressed by a highly variable and in all cases substantial difference between their ^{206}Pb/^{238}U and ^{208}Pb/^{232}Th ages. As seen from Figure 7e and Table 3, the ^{206}Pb/^{238}U ages are older by 1.8 to 6.3 Ma than the corresponding Th-Pb ages, with the oldest sample showing the largest offset.

The conservation of such a record relating to initial radioactive disequilibrium in ^{230}Th/^{238}U is of major importance for the interpretation of our allanite ages (von Blanckenburg, 1992; Oberli et al., 1996), provided that the enrichment in ^{206}Pb is not an artifact generated by a different process (see next section). Because it would take only 0.3 Ma for 94% of excess ^{230}Th to decay, residence of allanite above its closure temperature for a similar length of time would have caused the loss of an equivalent fraction of excess ^{230}Th produced radiogenic ^{206}Pb. The remaining 6% would result in age offsets of ≤0.4 Ma. In this case, the ^{206}Pb/^{238}U ages of most of the analyzed allanites would not be resolved from the corresponding ^{208}Pb/^{232}Th ages. The preservation of a well-resolved initial disequilibrium signature is therefore a prime argument for the interpretation of the Th-Pb data in terms of crystallization ages.

For minerals such as zircon, which have low Th/U as compared to their source, disequilibrium-induced ^{206}Pb/^{238}U age bias is confined to values between 0 ka (no fractionation of Th/U) and −109 ka, the mean life of ^{230}Th ($[Th/U]_{mineral} \sim 0$; Barth et al., 1994). Due to the relatively low Th content of the Bergell zircons, their Th-Pb data would not be precise enough to resolve age differences ≤109 ka. Furthermore, the resolution of the present ^{207}Pb/^{235}U data is not sufficient for resolving potential bias between the ^{206}Pb/^{238}U and ^{207}Pb/^{235}U ages. In contrast to allanite, insufficient analytical resolution prevents us here from using isotopic information intrinsic to zircon for distinguishing crystallization ages from closure ages. Similar arguments also hold for the titanite data.

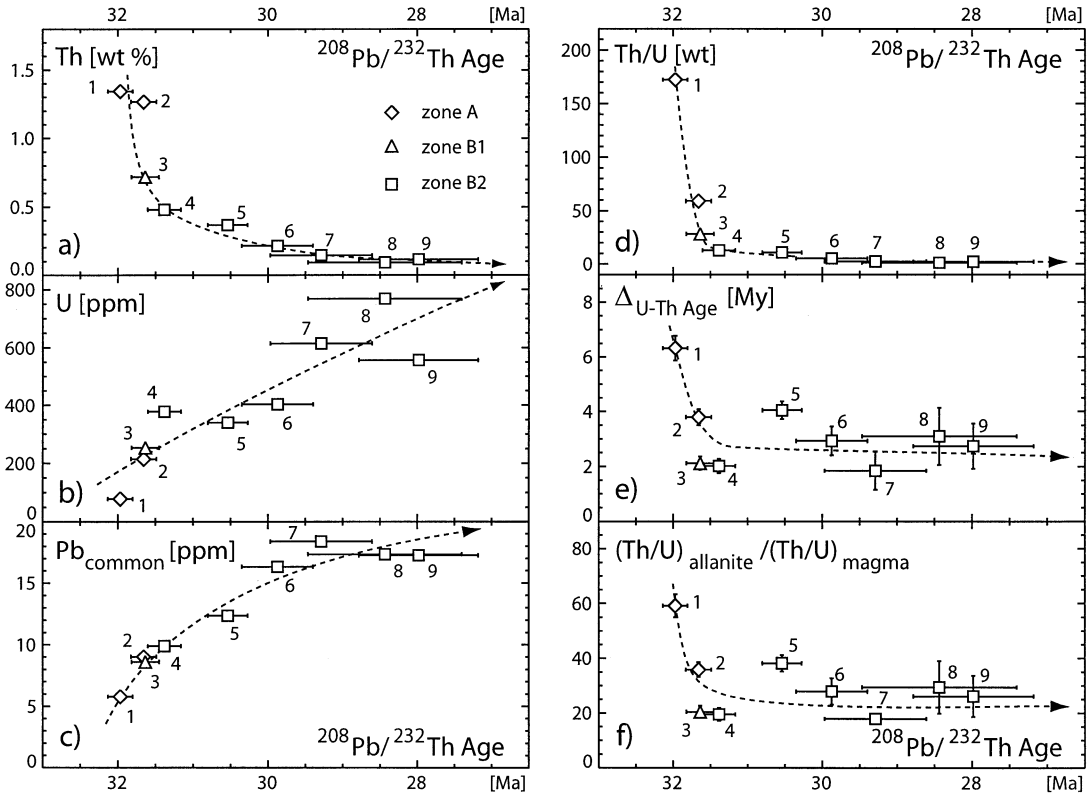

Fig. 7. (a–d) Plot of Th, U and Pb concentrations and Th/U vs. $^{208}Pb/^{232}Th$ age for density separated allanite fragments. The Th-Pb ages define an extended crystallization interval of 4 Ma (see text). The marked decrease of Th and increase of U and Pb concentrations with decreasing age are interpreted to mirror incompatible element concentration in an evolving melt. (e, f) Difference between $^{206}Pb/^{238}U$ and $^{208}Pb/^{232}Th$ age and solid/liquid fractionation coefficient for Th/U (see text). Positive age differences of 2 to 6 Ma between the U-Pb and Th-Pb ages for all analyses are proof for preservation of excess ^{230}Th-derived radiogenic ^{206}Pb, which excludes major resetting of the U-Th-Pb isotopic system in allanite after crystallization.

6.4. Th-U-Pb Isotope Disequilibrium Signature in Zoned Allanite: Real or Artifact?

Because presence of excess ^{206}Pb is clearly a prerequisite for interpreting the allanite ages in terms of crystallization ages, we need to demonstrate that the observed disequilibrium signature and the decrease in both Th-Pb and U-Pb ages from core to rim is not simply an artifact resulting from redistribution of radiogenic Pb within the crystals, with net loss to the matrix. The strong antithetic zoning of Th and U concentrations and associated non-homogeneous spatial production of radiogenic ^{208}Pb and ^{206}Pb (and ^{207}Pb) provide the basis for the rejection of such a hypothesis. Adopting a volume diffusion model as a proxy for Pb transport in allanite, we will show that postcrystallizational Pb loss would lead to an isotopic pattern grossly different from the observed one.

As diffusion tends to flatten concentration gradients, radiogenic ^{208}Pb produced in the Th rich cores of the allanites would preferentially move towards the rims, whereas part of ^{238}U produced ^{206}Pb from the U rich rims would migrate to the cores, which are lower in U and thus have produced less ^{206}Pb. This would lead to a net decrease of the $^{208}Pb/^{206}Pb$ ratio in the cores and therefore enhance their $\Delta_{U\text{-}Th\ Age}$, mimicking an initial disequilibrium signature. At the outer zones, however, $^{208}Pb/^{206}Pb$ would be expected to increase, resulting in Th-Pb ages older than the respective $^{206}Pb/^{238}U$ ages. This is in contrast to the observation, that in *all* zones the $^{206}Pb/^{238}U$ ages exceed corresponding $^{208}Pb/^{232}Th$ ages.

For a more rigid assessment of potential Pb mobility effects on our allanite samples, factors other than relative distribution of Th and U concentrations alone become important. These are (1) mass balance (core volumes are considerably smaller than rim volumes), (2) radiogenic Pb contributions by decay of U and Th *during* the process, and (3) ^{206}Pb production from decay of excess initial ^{230}Th. To quantify the U-Th-Pb isotopic data pattern that would result from subjecting an instantaneously grown zoned allanite crystal to open-system behavior during a cooling history such as might apply to the Bergell intrusion, we have performed numerical diffusion modeling, which takes into account all the factors mentioned above.

For simplicity, an orthorhombic crystal shape with diameters of 0.8, 3.2 and 1.6 mm along the *a*, *b* and *c* axes, respectively, was chosen for the calculations, approximately similar to the observed dimensions of the (monoclinic) allanite crystal depicted in Figure 4. Adopted zone dimensions and zonal distri-

bution of Th and U concentrations are shown in Figure 8a for the *a* axis and are based on both, EPMA and isotope dilution data; the zone dimensions along the *b* and *c* axes were scaled in proportion to the axial diameters. Because measured diffusion constants are not available for allanite, constants experimentally determined for titanite ($D_o = 1.11\ cm^2\ s^{-1}$ and $E_A = 78.5$ kcal mol^{-1}; Cherniak, 1993) were used instead. Dahl (1997) has suggested that the diffusion behavior of allanite might be similar to that of titanite, based on similar ionic porosity. However, we need to clearly state that these specific diffusion parameters have been selected for the sole purpose of providing diffusivities sufficiently high for Pb to behave as a mobile element at magmatic temperatures and during early cooling, such that the diffusion profiles resulting from the model calculations (Fig. 8b) can be compared with the observed U-Th-Pb isotopic pattern.

The temperature-time profile used for modeling (Fig. 8c) is based on the assumption that at 33 Ma (oldest zircon ages) the magma was at 750°C and cooled to 650°C (tonalite solidus at 0.8 GPa) by 26 Ma (epidote age) and to 320°C at 21 Ma (biotite K-Ar age; Villa and von Blanckenburg, 1991). In this model zoned allanite crystallizes instantaneously at 32.5 Ma (mean zircon age) at a magmatic temperature of 742°C. Initial (excess) concentrations of ^{230}Th were calculated from measured Th/U in allanite, adopting Th/U = 3 for the magma (justification follows in section 6.6). Complementary information on the computing procedures applied can be found in the Appendix.

The apparent ^{232}Th-^{208}Pb and ^{238}U -^{206}Pb age patterns resulting from diffusion modeling are presented in Figure 8b. They show both, similarities and marked dissimilarities with regard to the measured data. The mean Th-Pb ages of core zones A and B1 are lowered from 32.5 to 29.6 and 29.3 Ma by loss of ^{208}Pb, respectively, whereas the age raises to 32.2 Ma in zone B2. This latter feature has no equivalent in the real data pattern (Fig. 7). The low Th contents of zones C and D lead to an even more dramatic increase in the model Th-Pb age. Due to low actinide contents, however, no measurements are available for these outer zones.

As expected, the model yields *apparent* disequilibrium signatures in core zones A and B1 where the ^{238}U -^{206}Pb ages exceed corresponding ^{232}Th -^{208}Pb ages by 4.5 and 2.1 Ma, respectively (curve labeled $\Delta_{\text{U-Th Age}}$ in Fig. 8b). While the age offsets generated by the model are quite similar to the observed values (Fig. 7e), they are here solely a result of diffusional redistribution of ^{208}Pb and ^{206}Pb. Due to the particular choice of diffusion parameters, excess ^{230}Th produced ^{206}Pb is totally lost subsequent to crystallization, as the model crystal grows above its closure temperature.

The slope of the curve representing $\Delta_{\text{U-Th Age}}$ in Figure 8b becomes successively steeper from core to rim, whereas the opposite is observed for the real data (Fig. 7e). The absence of negative $\Delta_{\text{U-Th Age}}$ (i.e., Th-Pb age > U-Pb age) values for the outer zones of the measured crystals and the observed *continuous decrease* of the Th-Pb ages from core to rim are thus not compatible with major migration of Th and U derived ^{208}Pb and ^{206}Pb within the crystals.

Resetting of the Th-U-Pb isotopic system in allanite by a temperature-controlled volume diffusion mechanism is therefore not a tenable explanation for the observed spread of the Th-Pb ages. We thus conclude that the measured Th-Pb ages

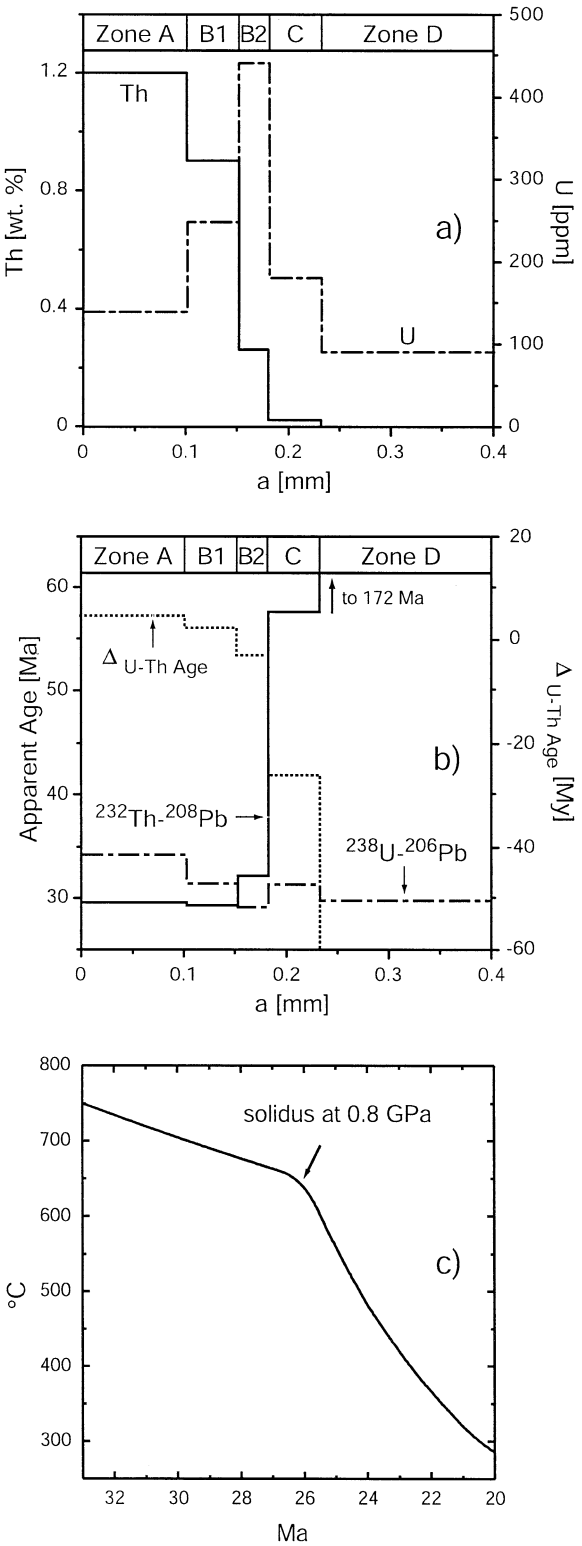

Fig. 8. Diffusion modeling for compositionally zoned allanite (see text and appendix for details): (a) Th (solid line) and U (dashed-dotted line) concentration profiles are shown for the *a* axis of the model crystal (0 mm = center of crystal); (b) apparent ^{232}Th-^{208}Pb (solid line) and ^{238}U-^{206}Pb (dashed-dotted line) age profiles resulting from integration of 3-D diffusion results within each separate zone; the dotted line represents the difference between the U-Pb and Th-Pb ages ("excess age"); (c) temperature-time profile used for modeling.

date magmatic allanite growth over a period of ~4 Ma. If this conclusion is valid, allanite has retained radiogenic Pb at temperatures ≥700°C (section 6.1). This then requires a closure temperature in excess of 700°C.

The apparent Th-Pb age of 31.6 Ma calculated for the bulk model crystal in combination with the adopted temperature-time profile yields an integral (apparent) closure temperature of 728°C for diffusion of ^{208}Pb. If similar model calculations are carried out for an unzoned crystal of similar size, the apparent Th-Pb age becomes 29.7 Ma, corresponding to a closure temperature of 700°C for ^{208}Pb. A calculation based on the zonal U distribution pattern shown in Figure 8a results in an apparent U-Pb age of 30.1 Ma and a related closure temperature of 706°C for ^{206}Pb. The higher apparent closure temperature for ^{232}Th derived ^{208}Pb in the zoned crystal as opposed to an unzoned crystal is due to the longer average diffusion distance to the matrix, when diffusant species production is concentrated in the center of a crystal. While laboratory diffusion experiments can avoid bias from zoning by selection of homogenous crystals, field based closure temperature estimates for accessory minerals may not always be safe from such effects.

6.5. Mineral Age Sequence

The observed regular increase of U concentration with decreasing age of the zircons has led to the conclusion that their disequilibrium corrected ^{206}Pb/^{238}U ages are valid approximations to the (integral) *crystallization* age of the abraded crystals. As the youngest zircon age (32.0 Ma) is identical with the oldest Th-Pb age measured for allanite, the zircon dates apparently trace the earlier part of a continuous crystallization history, which thus extends the magma evolution interval documented by both minerals to ~5 Ma. The absence of any correlation between Th/U ratio (Table 2) and U-Pb age of zircon suggests that the strong Th fractionation process associated with fractional crystallization of allanite was not yet operative when zircon crystallized.

The U-Pb ages of ~29.8 to 29.9 Ma obtained for titanite fall into the middle of the time segment occupied by the Th-Pb data of allanite. Relatively low Th/U (Table 2) suggests that these titanites crystallized at a time when the magma was already substantially depleted in Th. This is in tune with the observation that titanite is found in zone B of allanite, but is absent from the innermost zone A.

If the grossly distinct U concentrations of the titanites reflect varying U concentration in a slowly evolving magma environment, then the narrow time interval occupied by their U-Pb ages would have to be explained by near-simultaneous closure upon cooling rather than by crystallization during a narrow time interval. Calculations based on the diffusion parameters $D_o = 1.11$ cm^2 s^{-1} and $E_A = 78.5$ kcal mol^{-1} determined by Cherniak (1993) for non-metamict titanite, however, are in conflict with this hypothesis. For a cooling rate of 14°C Ma^{-1} (cf. Fig. 8c and text), closure temperatures of 706 and 637°C are obtained for titanite samples ti1 (0.8 mm thickness before abrasion; plane sheet geometry) and ti3 (0.28 mm; cylindrical geometry) respectively, using the volume diffusion model of Dodson (1973). Taking into account the reduction of grain thickness by abrasion (to 0.4 mm for ti1 and 0.24 mm for ti3), closure temperatures representative for the abraded grains increase to 730 and 654°C, respectively, as obtained from numerical integration of the closure temperature distribution function of Dodson (1986). If these grain sizes are valid approximations for the effective diffusion domain diameters, then the difference of ~80°C between the calculated closure temperatures of the two samples is grossly incompatible with the assumed cooling rate of 14°C Ma^{-1} and a maximum U-Pb age difference of ~0.2 Ma derived from their extreme error bounds (see Table 3). It is therefore possible that the titanite ages date crystallization below closure temperature and that closure temperatures >700°C, as constrained by the stability field of allanite (section 6.1), may be more realistic for grain diameters of ~0.24 mm than the lower values calculated from the diffusion parameters provided by Cherniak (1993). Such an interpretation would also better match minimum closure temperature estimates of 660 to 700°C for ≥50-μm-sized titanites by Scott and St-Onge (1995), but remains at variance with earlier, lower estimates of ~600°C based on multiple observations on the resetting behavior of the U-Pb system in titanite under high-grade metamorphic conditions (Heaman and Parrish, 1991).

Similarly, the meaning of the young apparent U-Pb age of 25.7 ± 1.1 Ma obtained from a single epidote analysis is not clear. Due to uncertain textural context and lack of precise ^{230}Th/^{238}U disequilibrium related information, this sample does not provide sufficient criteria to distinguish between a primary crystallization age, an age reset by loss of radiogenic Pb, or even growth related to solid state reactions during high-grade regional metamorphism. More detailed work is required to finally solve these issues.

6.6. The Evolution of the Melt

A fractionation factor $f = (\mathrm{Th/U})_{\mathrm{allanite}} / (\mathrm{Th/U})_{\mathrm{magma}}$ can readily be calculated from the relation $\Delta_{\mathrm{U\text{-}Th\ Age}} \approx (1/\lambda_{230})(f - 1)$ (Barth et al., 1994) and the corresponding values listed in Table 3. $\Delta_{\mathrm{U\text{-}Th\ Age}}$ is the difference between the (apparent) ^{206}Pb/^{238}U age and the (true) ^{208}Pb/^{232}Th age as defined in section 6.4, and $1/\lambda_{230}$ is the mean life of ^{230}Th (109 ka). For simplicity of presentation we first assume that ^{230}Th/^{238}U in the magma remains at secular equilibrium during fractionation, a rather unrealistic assumption to be refined below. We note that the calculated f values (Table 3 and Fig. 7f) are rather variable and show considerable scatter, probably due to Th-U partitioning being modified by changes in allanite and evolving melt composition.

From f and measured Th/U in allanite (Table 2 and Fig. 7d), Th/U of the magma in equilibrium with the individual allanite zones can then be derived (Table 3). A plot of $(\mathrm{Th/U})_{\mathrm{magma}}$ vs. Th-Pb age of the corresponding zones results in a surprisingly smooth evolution curve (Fig. 9), considering the scatter exhibited by the f values in Figure 7f. $(\mathrm{Th/U})_{\mathrm{magma}}$ monotonously decreases from 2.9 at 32 Ma to very low values of ~0.04 to 0.08 at ~28.4 to 28.0 Ma. The value of 2.9 obtained for the oldest allanite sample (a1) is much closer to Th/U = 3.2 measured for the least evolved magmatic member associated with the Bergell intrusion (basaltic dyke Malf 1; von Blanckenburg et al., 1992) than the rather low measured total-rock value of 0.79 (cf. Table 1) represented by the dashed line in Figure 9.

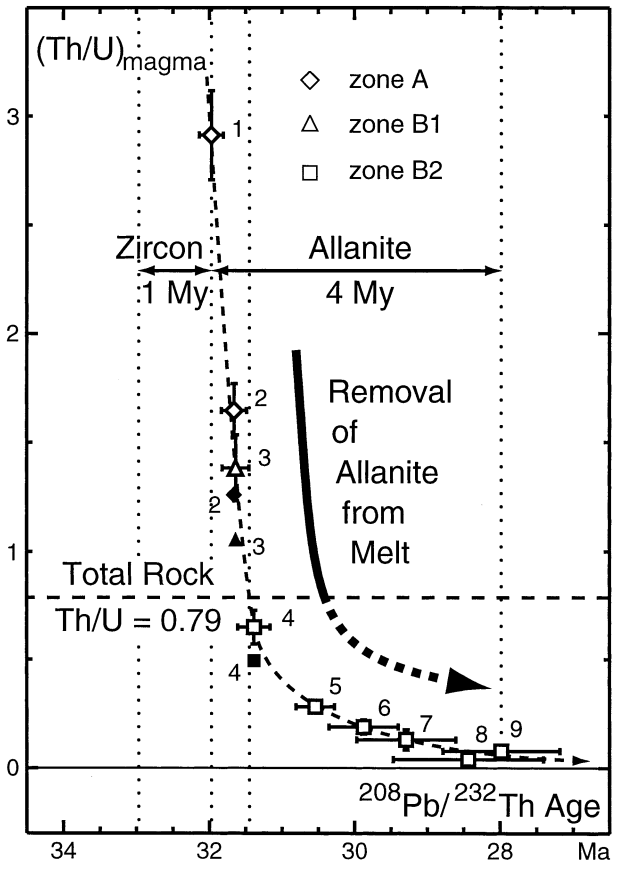

Fig. 9. Evolution of Th/U in the magma versus time calculated from the allanite data shown in Figures 7d to 7f. Open and solid symbols (the latter shown only when not overlapping the former) denote data points uncorrected and corrected for disequilibrium in $(^{230}Th/^{238}U)_{magma}$, respectively (see text and Table 3; labels refer to the corresponding sample numbers).

Because Th/U in the melt in equilibrium with early allanite was >3 times higher than the measured total-rock value, the magma must have undergone *fractional crystallization before emplacement,* as cumulate textures are not observed at the sampling locality. A large fraction of allanite must have been physically removed from the melt *after* the oldest measured allanite components had crystallized. An upper limit of ~31.4 Ma for the end of open-system fractional crystallization and thus emplacement is given by the intersection of the fractionation curve with total-rock Th/U = 0.79. This age however, would only approximate the real intrusion age if the oldest allanite components in the sample were in equilibrium with total-rock Th/U, or, with other words, if there were no data points above the total-rock line in Figure 9. Because the intruding magma did carry early allanite crystals characterized by high Th/U ratios, Th/U in the melt fraction of the magma at 31.4 Ma must have been lower than the measured total rock-value which in turn requires the emplacement, or real intrusion, age to be younger than 31.4 Ma.

We note that at ~31.4 Ma, there is a pronounced change in the slope of the line of $(Th/U)_{magma}$ vs. time in Figure 9. This change coincides with the transition from zone B1 to zone B2 in allanite. Whereas Th/U drops very rapidly before this time, indicative of a relatively high crystallization rate for allanite, the rate of change becomes much lower afterwards. This observation can tentatively be interpreted in terms of rapid ascent of the magma from lower crustal levels accompanied by fast cooling and crystallization, followed by slower cooling rates after emplacement into hot country rock.

Alternatively, a transition from a magmatic crystallization regime to postemplacement subsolidus growth in a regional high-grade metamorphic environment could also result in a change (or break) of slope for Th/U, depending on the source(s) supplying these trace elements. However, the change in curvature of Th/U_{magma} vs. time appears to be continuous rather than representing a break. Furthermore, the magmatic textural relationship between the allanite cores and the epidote rims, the smooth trend in REE + Th vs. Al (Fig. 5) and the systematic shift in the REE patterns (Fig. 6) are all in favor of the former interpretation.

Disequilibrium in $(^{230}Th/^{238}U)_{magma}$ resulting from preferential extraction of ^{230}Th by allanite crystallization has not been taken into account for calculation of the $(Th/U)_{magma}$ values listed in Table 3 and shown in Figure 9 (open symbols). This leads to underestimation of f and consequently to overestimation of calculated $(Th/U)_{magma}$. To assess the effect of melt disequilibrium on the position of the $(Th/U)_{magma}$ evolution curve in Figure 9, a rough two-stage calculation was carried out, using $(Th/U)_t \approx (Th/U)_0 \times \exp(k \times t)$ for fitting (calculated) Th/U evolution in the magma, with t denoting the time in million years elapsed since the start of stage 1 (chosen to last from 32.0 to 31.3 Ma) and stage 2 (31.3–28.0 Ma), respectively. For stage 1, we adopted $(Th/U)_0 = 2.9$, with $^{230}Th/^{238}U$ initially at equilibrium, and $k = k_1 = -3.0\ Ma^{-1}$. For stage 2, k was decreased to $k_2 = -0.5\ Ma^{-1}$. The calculations show that for this parameter set the $^{230}Th/^{238}U$ activity ratio in the melt rapidly drops from the initial value of 1.0 at 32.0 Ma to a steady-state value of ~0.75 for the time interval of ~31.6 to 31.3 Ma, and then, in response to the change of fractionation rate at the start of the second stage (31.3 Ma) forced by the model, again reaches a steady-state value of ~0.95 at ~30.8 Ma. If the deviation of the activity ratio in the melt from unity is taken into account for calculation of $(Th/U)_{magma}$, the data points corresponding to samples a2, a3 and a4 shift to lower values (see Table 3 and Fig. 9, solid symbols), whereas the offsets of the other data points are negligible. We further note that the intercept of the data array with total-rock Th/U is only minimally shifted from ~31.4 to ~31.5 Ma.

Independent evidence for removal of substantial amounts of allanite from the melt is also provided by the total-rock Sm-Nd data listed in section 5.5. In Sr-Nd isotope space, these data plot within the tonalite segment of the data array defined by major Bergell lithologies (von Blanckenburg, 1992; von Blanckenburg et al., 1998). Sm/Nd = 0.30 in our sample, however, is anomalously high for a differentiated crustal rock (typical range: ~0.15–0.20) and also exceeds the range of 0.17 to 0.23 observed in the tonalites analyzed by the above authors. Whereas the Sm concentration of our sample (4.0 ppm) conforms to the lower end of the concentration range defined by their data (3.9–7.5 ppm), its Nd concentration of 13.5 ppm is clearly below the values measured for the other tonalites (16.8–43 ppm). In the present context, high bulk-rock Sm/Nd

combined with low Nd concentration is best explained in terms of LREE depletion by fractional crystallization of allanite commencing at an early magmatic stage (cf. Fig. 6). Among the mafic cumulate rocks described from the Bergell suite (von Blanckenburg, 1992), allanite-rich members, however, have not been discovered so far. This can be explained by the large density contrast between allanite and less dense hornblende and pyroxene, which may have prevented joint accumulation of these phases in cumulates.

6.7. The "Age" of the Bergell Intrusion and Its Implications

Taken together, the zircon and allanite age results from the western margin of the intrusion document an extended magmatic crystallization history, lasting from 33 until ~28 Ma, with epidote possibly forming as late as 26 Ma. Th-U-Pb isotope systematics require that zircon and allanite Th-Pb ages older than ~31.5 Ma date crystallization in a fractionating magma chamber, whereas emplacement and solidification of the evolved magma batch represented by the bulk sample must postdate this time marker.

The existence of analytically resolved crystallization intervals totaling at least 5 Ma recorded within the deep-seated westernmost part of the Bergell intrusion and, in particular, a time span of ≥1.5 Ma between the onset of zircon crystallization and the end of open-system fractional crystallization suggest prolonged residence in a slowly evolving magma chamber, probably located within the lower crust (von Blanckenburg et al., 1998). We note that this time span is exceptionally long compared to "typical" magma residence times of 10^1 to 10^5 yr estimated by a variety of methods for volcanic melts (see Hawkesworth et al., 2000, and references therein), or even 0.7 Ma as inferred from Rb-Sr isochron measurements applied to high-silica lavas (Halliday et al., 1989).

In view of the great difference between the intrusion levels of the eastern and the western parts of the pluton (Davidson et al., 1996; Reusser, 1987), it is of interest, to what extent magma crystallization and emplacement may have been synchronous or asynchronous over the length of the pluton. Three zircon analyses published by von Blanckenburg (1992) for a tonalite from the shallower (0.3–0.5 GPa) easternmost margin of the intrusion were performed on samples composed of 3 to 10 grains each and gave reproducible, disequilibrium-corrected $^{206}Pb/^{238}U$ ages between 31.80 and 31.96 Ma (±0.14–0.17 Ma). These ages are younger than most of the zircon ages listed in Table 3, but overlap within error limits with the age of sample z5 (32.02 ± 0.12 Ma). There is also a hint of correlation between increasing U content and decreasing $^{206}Pb/^{238}U$ age of the samples, although statistically not significant and possibly masked by the averaging effect of multi-grain analysis. Because the zircons from the E Bergell were not abraded and thus may have been biased towards younger ages in comparison to our data, we cannot exclude the possibility that the zircon populations at both ends of the pluton—60 km apart—may have crystallized synchronously during the same magma chamber stage.

This possibility also extends to allanite, because the Th-Pb age of 31.50 ± 0.35 Ma (sample consisting of 30 allanite grains from the tonalite) reported by von Blanckenburg (1992) is identical within error limits to the ages of our allanite samples a3 (31.64 ± 0.18 Ma) and a4 (31.38 ± 0.22 Ma), composed of 9 to 10 grains each and similarly picked from the bulk concentrate. In the granodioritic lithology confined to the eastern part of the pluton, allanite and magmatic titanite gave $^{208}Pb/^{232}Th$ and $^{206}Pb/^{238}U$ ages of 30.10 ± 0.25 and of 30.16 ± 0.24 Ma, respectively (von Blanckenburg, 1992). These identical ages postdate the zircon ages from the eastern tonalite by 1.5 to 1.8 Ma and were thus interpreted in terms of a younger intrusion age for the granodiorite, consistent with field observations. The ages, however, are only slightly older than the three titanite ages of ~29.8 to 29.9 Ma obtained for the W Bergell tonalite (Table 3). In view of the similarities in most of the ages from both ends of the pluton it is possible that the dated lithologies may have shared a similar history of magmatic evolution and emplacement. In this case, the zircons and allanites from the eastern tonalite would also predate the emplacement of their host rock.

The persistence of a large crustal magma chamber for >1.5 Ma, as indicated by our data, is consistent with the extended polyphase emplacement and folding history of the pluton. Ascent of fractionated crystal bearing magma resulted in a first emplacement stage on top of the lower Penninic country rocks and was followed by a magmatic folding phase (Rosenberg et al., 1995; Berger et al., 1996; Davidson et al., 1996). Structural data from the eastern margin of the pluton, where the intrusives were in contact with colder country rocks, indicate ballooning between 32 and 30 Ma (Rosenberg et al., 1995; Berger et al., 1996). At this time, the roof of the pluton was already solidifying, whereas at the deeper and hotter crustal levels near the western margin, the pluton still remained in the molten state, probably until ~28 Ma (youngest Th-Pb age on allanite). It has been demonstrated by thermal modeling that magmas intruding hot crustal regions may remain in a partially molten state for up to several million years (e.g., Davidson et al., 1992). The Southern Steep Belt then remained thermally active at least until 25 Ma as documented by zircon ages of S-type granites and pegmatites (see Liati et al., 2000, and references therein).

7. CONCLUSIONS

Conventional high-resolution U-Th-Pb isotope techniques and complementary mineralogical observations applied to a single rock sample from a large calc-alkaline pluton have documented several million years of melt evolution and crystallization. We have demonstrated that our age results obtained on zircon, density-separated allanite and titanite relate to finite time intervals of melt fractionation, emplacement and in situ crystallization rather than simply dating a short-lived single magmatic pulse. Complementary isotope-geochemical arguments rather than age data alone were required to constrain the intrusion age, a time marker essential to models of crustal dynamics. The results of our study caution against indiscriminate equation of isotopic ages with intrusion/cooling ages. As ongoing progress in dating techniques allows investigation of ever younger magmatic systems to ever greater analytical resolution, the exact significance of isotopic ages becomes more and more a critical issue.

For the interpretation of our results, we have made extensive

use of isotope systematics *intrinsic* to the U-Th-Pb systems of the samples analyzed. For zoned allanite, the combination of the Th-Pb dating technique with conventional U-Pb dating does not only result in a sequence of precise crystallization ages, which span a range of 4 Ma (32–28 Ma), but also proves that the observed age sequence is not merely an artifact of syn- or postmagmatic open-system behavior. The presence of excess initial ^{230}Th derived ^{206}Pb in *all* growth zones at widely varying Th/U suggests that the isotopic ages have not suffered major resetting by diffusion of radiogenic Pb.

Following an early evolution interval of 1 Ma (33–32 Ma) defined by zircon U-Pb, the onset of allanite crystallization led to a continuous decrease of Th/U in the melt spanning a time interval of ~4 Ma (32–28 Ma). This process, traced and dated by Th-U-Pb isotope data, is accompanied by a change in REE characteristics, from the highly LREE enriched cores to an essentially flat REE distribution at the allanite rims. The preservation of this regular magmatic fractionation pattern corroborates our conclusion that the investigated grains approach closed-system behavior in their mineralogical as well as in their isotopic characteristics. Consequently, the closure temperature of the Bergell allanites had to be ≥700°C, exceeding the value of 650 ± 25°C derived by Heaman and Parrish (1991). This difference could indicate that estimates based on magmatic assemblages might systematically be offset from those obtained on metamorphic settings. A comparison of Th-U-Pb isotope systematics in allanite with whole rock Th/U further implies that before the emplacement at the present sampling location at <31.5 Ma, magma evolution was controlled by *open-system* fractional crystallization in a magma chamber.

Special thermal conditions are required to keep magmatic systems active for ~5 Ma. We believe the extremely long duration of magmatic evolution and crystallization recorded by our sample to be a consequence of prolonged residence in a deep-seated magma chamber and emplacement into hot, deeply buried crust at ≥0.8 GPa. Elevated temperatures caused by the proximity of a mantle heat source, heat advection by passage of large volumes of magma through the feeder channel forming the main, later eroded, plutonic body atop of this zone, and a thermal cushion provided by liberation of latent heat from the crystallization of the intrusion, were probably responsible for maintaining magmatic conditions from ~33 until ~28 Ma. The persistence of melt from <31.5 until ~28 Ma at the intrusive level, capable of focusing strain into a narrow zone at the interface of two major plates, emphasizes the role of the Periadriatic fault system as the major tectonic controlling factor for the Oligocene evolution of the Eastern Central Alps.

Acknowledgments—We would like to thank H. Derksen and W. Wittwer for support in mineral separation and E. Reusser for providing access to the electron microprobe at IMP ETH Zurich. We are grateful to W. B. Stern for XRF concentration data and to Y. C. Lavanchy for a determination of FeO in total rock. H. Baur, U. Derksen, U. Menet and B. Rütsche have provided invaluable technical support in mass spectrometry and computing. The manuscript has substantially benefited from constructive reviews by K. Mezger, R. R. Parrish and F. von Blanckenburg, and from editorial comments by S. J. G. Galer.

Associate editor: S. J. Galer

REFERENCES

Amelin Y. and Zaitsev A. N. (2002) Precise geochronology of phoscorites and carbonatites: The critical role of U-series disequilibrium in age interpretations. *Geochim. Cosmochim. Acta* **66,** 2399–2419.

Anczkiewicz R., Oberli F., Burg J. P., Villa I. M., Günther D., and Meier M. (2001) Timing of normal faulting along the Indus Suture in Pakistan Himalaya and a case of major ^{231}Pa/^{235}U initial disequilibrium in zircon. *Earth Planet. Sci. Lett.* **191,** 101–114.

Barth S., Oberli F., and Meier M. (1989) U-Th-Pb systematics of morphologically characterized zircon and allanite; a high-resolution isotopic study of the Alpine Rensen Pluton (northern Italy). *Earth Planet. Sci. Lett.* **95,** 235–254.

Barth S., Oberli F., and Meier M. (1994) Th-Pb versus U-Pb isotope systematics in allanite from co-genetic rhyolite and granodiorite: Implications for geochronology. *Earth Planet. Sci. Lett.* **124,** 149–159.

Berger A. and Stuenitz H. (1996) Deformation mechanisms and reaction of hornblende; examples from the Bergell tonalite (Central Alps). *Tectonophys.* **257,** 149–174.

Berger A., Rosenberg C., and Schmid S. M. (1996) Ascent, emplacement and exhumation of the Bergell pluton within the Southern Steep Belt of the Central Alps. *Schweiz. Mineral. Petrogr. Mitt.* **76,** 357–382.

Catlos E. J., Sorensen S. S., and Harrison T. M. (2000) Th-Pb ion-microprobe dating of allanite. *Am. Mineral.* **85,** 633–648.

Cherniak D. J. (1993) Lead diffusion in titanite and preliminary results on the effects of radiation damage on Pb transport. *Chem. Geol.* **110,** 177–194.

Cherniak D. J. and Watson E. B. (2000) Pb diffusion in zircon. *Chem. Geol.* **172,** 5–24.

Copeland P., Parrish R. R., and Harrison T. M. (1988) Identification of inherited radiogenic Pb in monazite and its implications for U-Pb systematics. *Nature* **333,** 760–763.

Dahl P. S. (1997) A crystal-chemical basis for Pb retention and fission-track annealing systematics in U-bearing minerals, with implications for geochronology. *Earth Planet. Sci. Lett.* **150,** 277–290.

Davidson C., Hollister L. S., and Schmid S. M. (1992) Role of melt in the formation of a deep-crustal compressive shear zone; the Maclaren Glacier metamorphic belt, south central Alaska. *Tectonics* **11,** 348–359.

Davidson C., Rosenberg C., and Schmid S. M. (1996) Synmagmatic folding of the base of the Bergell Pluton, Central Alps. *Tectonophys.* **265,** 213–238.

Dodson M. H. (1973) Closure temperature in cooling geochronological and petrological systems. *Contrib. Mineral. Petrol.* **40,** 259–274.

Dodson M. H. (1986) Closure profiles in cooling systems. *Mat. Sci. Forum* **7,** 145–154.

Engi M., Todd C. S., and Schmatz D. R. (1995) Tertiary metamorphic conditions in the eastern Lepontine Alps. *Schweiz. Mineral. Petrogr. Mitt.* **75,** 347–369.

Farmer G. L. and DePaolo D. J. (1983) Origin of Mesozoic and Tertiary granite in the Western United States and implications for pre-Mesozoic crustal structure 1. Nd and Sr isotopic studies in the geocline of the Northern Great Basin. *J. Geophys. Res.* **88,** 3379–3401.

Gebauer D. (1999) Alpine geochronology of the Central and Western Alps: New constraints for a complex geodynamic evolution. *Schweiz. Mineral. Petrogr. Mitt.* **79,** 191–208.

Gieré R. and Stahel A. (1996) Transition from Penninic to Austroalpine units in the Bergell Alps: Introduction. *Schweiz. Mineral. Petrogr. Mitt.* **76,** 325–328.

Giger M. (1991) *Geochronologische und petrographische Studien an Geröllen und Sedimenten der Gonfolite Lombarda Gruppe (Südschweiz und Norditalien) und ihr Vergleich mit dem alpinen Hinterland*. Ph.D. thesis, Bern University.

Giger M. and Hurford A. J. (1989) Tertiary intrusives of the Central Alps; their Tertiary uplift, erosion, redeposition and burial in the south-alpine foreland. *Eclogae Geol. Helv.* **82,** 857–866.

Grünenfelder M. and Stern T. W. (1960) Das Zirkon-Alter des Bergeller Massivs. *Schweiz. Mineral. Petrogr. Mitt.* **40,** 253–259.

Gulson B. L. and Krogh T. E. (1973) Old lead components in the young Bergell massif, South-East Swiss Alps. *Contrib. Mineral. Petrol.* **40,** 239–252.

Hafner M. (1993) *Strukturgeologische und geochemische Untersuchungen von leukokraten Granit-Gängen und Migmatiten der südlichen Adula am Monte Peschiera (It.)*. Diploma thesis, Basel University.

Halliday A. N., Mahood G. A., Holden P., Metz J. M., Dempster T. J., and Davidson J. P. (1989) Evidence for long residence times of rhyolitic magma in the Long Valley magmatic system—The isotopic record in precaldera lavas of Glass Mountain. *Earth Planet. Sci. Lett.* **94,** 274–290.

Hansmann W. (1996) Age determinations on the Tertiary Masino-Bregaglia (Bergell) intrusives (Italy, Switzerland): A review. *Schweiz. Mineral. Petrogr. Mitt.* **76,** 421–451.

Hansmann W. and Oberli F. (1991) Zircon inheritance in an igneous rock suite from the southern Adamello batholith (Italian Alps). Implications for petrogenesis. *Contrib. Mineral. Petrol.* **107,** 501–518.

Hawkesworth C. J., Blake S., Evans P., Hughes R., MacDonald R., Thomas L. E., Turner S. P., and Zellmer G. (2000) Time scales of crystal fractionation in magma chambers—Integrating physical, isotopic and geochemical perspectives. *J. Petrol.* **41,** 991–1006.

Heaman L. and Parrish R. (1991) U-Pb geochronology of accessory minerals. In *Applications of Radiogenic Isotope Systems to Problems in Geology, Short Course Handbook 19* (eds. L. Heaman and J. N. Ludden), pp. 59–102. Mineralogical Association of Canada, Toronto.

Huang W. L. and Wyllie P. J. (1986) Phase-relationships of gabbro-tonalite-granite-water at 15 kbar with applications to differentiation and anatexis. *Am. Mineral.* **71,** 301–316.

Krogh T. E. (1973) A low-contamination method for hydrothermal decomposition of zircon and extraction of U and Pb for isotopic age determinations. *Geochim. Cosmochim. Acta* **37,** 485–494.

Krogh T. E. (1982) Improved accuracy of U-Pb zircon ages by the creation of more concordant systems using an air abrasion technique. *Geochim. Cosmochim. Acta* **46,** 637–649.

Lambert I. B. and Wyllie P. J. (1974) Melting of tonalite and crystallization of andesite liquid with excess water to 30 kilobars. *J. Geol.* **82,** 88–97.

Lee J. K. W., Williams I. S., and Ellis D. J. (1997) Pb, U and Th diffusion in natural zircon. *Nature* **390,** 159–162.

Liati A., Gebauer D., and Fanning M. (2000) U-Pb SHRIMP dating of zircon from the Novate granite (Bergell, Central Alps): Evidence for Oligocene-Miocene magmatism, Jurassic/Cretaceous continental rifting and opening of the Valais trough. *Schweiz. Mineral. Petrogr. Mitt.* **80,** 305–316.

Mezger K. and Krogstad E. J. (1997) Interpretation of discordant U-Pb zircon ages: An evaluation. *J. Metamorph. Geol.* **15,** 127–140.

Mortensen J. K., Williams I. S., and Compston W. (1997) Ion microprobe and cathodoluminescence investigations of unsupported ^{207}Pb in zircon. In *GAC/MAC Ann. Meeting Abstr. Vol., Ottawa*, p. 105.

Oberli F., Meier M., Berger A., Rosenberg C., and Gieré R. (1996) ^{230}Th/^{238}U disequilibrium systematics in U-Th-Pb dating: Nuisance or powerful tool in geochronometry? *J. Conf. Abstr. V. M. Goldschmidt Conf.* **1,** 439.

Oberli F., Gartenmann P., Meier M., Kutschera W., Suter M., and Winkler G. (1999) The half-life of ^{126}Sn refined by thermal ionization mass spectrometry measurements. *Int. J. Mass Spect. Ion Proc.* **184,** 145–152.

Parrish R. R. (2001) The response of mineral chronometers to metamorphism and deformation in orogenic belts. In *Continental Reactivation and Reworking, Vol. 184* (eds. J. A. Miller, R. E. Holdsworth, I. S. Buick, and M. Hand), pp. 289–301. Geol. Soc, London.

Petrik I., Broska I., Lipka J., and Siman P. (1995) Granitoid allanite-(Ce): Substitution relations, redox conditions and REE distributions (on an example of I-type granitoids, Western Carpathians, Slovakia). *Geol. Carpathica* **46,** 79–94.

Poitrasson F. (2002) In situ investigations of allanite hydrothermal alteration: Examples from calc-alkaline and anorogenic granites of Corsica (Southeast France). *Contrib. Mineral. Petrol.* **142,** 485–500.

Pouchou J. L. and Pichoir F. (1984) Un nouveau modèle de calcul pour la microanalyse quantitative par spectrométrie de rayons X. Partie I: Application à l'analyse des échantillons homogènes. *Rech. Aérospatiale* **3,** 167–192.

Press W. H., Teukolsky S. A., Vetterling W. T., and Flannery B. P. (1992) *Numerical Recipes in C: The Art of Scientific Computing*. Cambridge University Press, Cambridge, UK.

Reusser C. E (1987) *Phasenbeziehungen im Tonalit der Bergeller Intrusion*. Ph.D. thesis, ETH Zürich.

Rosenberg C. L. and Heller F. (1997) Tilting of the Bergell Pluton and central Lepontine area: Combined evidence from paleomagnetic, structural and petrological data. *Eclogae Geol. Helv.* **90,** 345–356.

Rosenberg C. L., Berger A., and Schmid S. M. (1995) Observations from the floor of a granitoid pluton: Inferences on the driving force of final emplacement. *Geology* **23,** 443–446.

Schaltegger U. and Gebauer D. (1999) Pre-Alpine geochronology of the Central, Western and Southern Alps. *Schweiz. Mineral. Petrogr. Mitt.* **79,** 79–87.

Schärer U. (1984) The effect of initial ^{230}Th disequilibrium on young U-Pb ages: The Makalu case, Himalaya. *Earth Planet. Sci. Lett.* **67,** 191–204.

Schmid S. M., Aebli H. R., Heller F., and Zingg A. (1989) The role of the Periadriatic Line in the tectonic evolution of the Alps. *Geol. Soc. London Spec. Publ.* **45,** 153–171.

Schmidt M. W. and Thompson A. B. (1996) Epidote in calc-alkaline magmas: An experimental study of stability, phase relationships, and the role of epidote in magmatic evolution. *Am. Mineral.* **81,** 462–474.

Scott D. J. and St-Onge M. R. S. (1995) Constraints on Pb closure temperature in titanite based on rocks from the Ungava orogen, Canada: Implications for U-Pb geochronology and P-T-t path determinations. *Geology* **23,** 1123–1126.

Spear F. and Parrish R. (1996) Petrology and cooling rates of the Valhalla complex, Br. Columbia, Canada. *J. Petrol.* **37,** 733–765.

Todd C. S. and Engi M. (1997) Metamorphic field gradients in the Central Alps. *J. Metamorph. Geol.* **15,** 513–530.

Trommsdorff V. and Nievergelt P. (1983) The Bregaglia (Bergell) Iorio intrusive and its field relations. *Mem. Soc. Geol. It.* **26,** 55–68.

Villa I. M. and von Blanckenburg F. (1991) A hornblende ^{39}Ar-^{40}Ar age traverse of the Bregaglia tonalite (southeast Central Alps). *Schweiz. Mineral. Petrogr. Mitt.* **71,** 73–87.

von Blanckenburg F. (1992) Combined high-precision chronometry and geochemical tracing using accessory minerals: Applied to the Central-Alpine Bergell intrusion (central Europe). *Chem. Geol.* **100,** 19–40.

von Blanckenburg F., Früh-Green G., Diethelm K., and Stille P. (1992) Nd-, Sr-, O-isotopic and chemical evidence for a two-stage contamination history of mantle magma in the Central-Alpine Bergell intrusion. *Contrib. Mineral. Petrol.* **110,** 33–45.

von Blanckenburg F., Kagami H., Deutsch A., Oberli F., Meier M., Wiedenbeck M., Barth S., and Fischer H. (1998) The origin of Alpine plutons along the Periadriatic Lineament. *Schweiz. Mineral. Petrogr. Mitt.* **78 (*1*),** 55–66.

Wakita H., Rey P., and Schmitt R. A. (1971) Abundances of the 14 rare earth elements and 12 other elements in Apollo 12 samples: Five igneous and one breccia rocks and four soils. *Proc. Second Lunar Sci. Conf. Geochim. Cosmochim. Acta* **2 (*Suppl.*),** 1319–1329.

Wasserburg G. J., Jacobsen S. B., DePaolo D. J., McCulloch M. T., and Wen T. (1981) Precise determination of Sm/Nd ratios, Sm and Nd isotopic abundances in standard solutions. *Geochim. Cosmochim. Acta* **45,** 2311–2323.

Watson E. B. and Harrison T. M. (1983) Zircon saturation revisited—Temperature and composition effects in a variety of crustal magma types. *Earth Planet. Sci. Lett.* **64,** 295–304.

Wiedenbeck M., Allé P., Corfu F., Griffin W. L., Meier M., Oberli F., Von Quadt A., Roddick J. C., and Spiegel W. (1995) Three natural zircon standards for U-Th-Pb, Lu-Hf, trace element and REE analyses. *Geostand. News.* **19,** 1–23.

Williams C. T. (1996) Analysis of rare earth minerals. In *Rare Earth Minerals: Chemistry, Origin and Ore Deposits, Mineralogical Society Series 7* (eds. A.P. Jones, F. Wall, and C. T. Williams), pp. 327–348. Chapman and Hall, London.

APPENDIX

The change in concentration of radiogenic ^{206}Pb (c_{206}) with time t at a given crystal location can be described by the differential equation

$$\frac{dc_{206}}{dt} = \lambda_{230} \cdot c_{230}(t) + D(t) \cdot \left(\frac{\partial^2 c_{206}}{\partial x^2} + \frac{\partial^2 c_{206}}{\partial y^2} + \frac{\partial^2 c_{206}}{\partial z^2} \right) . \tag{A1}$$

The first term on the right hand side of Eqn. A1 describes the production of ^{206}Pb from radioactive decay of ^{230}Th, an intermediate long-lived radioactive daughter nuclide in the ^{238}U decay chain, where

$$\frac{dc_{230}}{dt} = \lambda_{238} \cdot c_{238}(t) - \lambda_{230} \cdot c_{230}(t) . \tag{A2}$$

where c_{230}, c_{238}, λ_{230} and λ_{238} denote concentrations and decay constants of ^{230}Th and ^{238}U, respectively.

The second term of Eqn. A1 relates to the diffusional change in ^{206}Pb concentration induced by concentration gradients in x, y and z. The diffusion coefficient D is a function of absolute temperature T, preexponential factor D_0 and activation energy E_A

$$D(t) = D_0 \cdot e^{-\frac{E_A}{R \cdot T(t)}} . \tag{A3}$$

T is interpolated between the temperature-time markers representing the cooling history (section 6.4, Fig. 8c) using constant $(dT/dt)^{-1}$ (Dodson, 1973).

For ^{232}Th derived ^{208}Pb, Eqn. A1 becomes

$$\frac{dc_{208}}{dt} = \lambda_{232} \cdot c_{232}(t) + D(t) \cdot \left(\frac{\partial^2 c_{208}}{\partial x^2} + \frac{\partial^2 c_{208}}{\partial y^2} + \frac{\partial^2 c_{208}}{\partial z^2} \right) . \tag{A4}$$

The symmetrically zoned model crystal was represented by 81 × 321 × 161 equally spaced grid points in x, y and z half axis direction. These were seeded with initial ^{238}U and ^{230}Th concentrations ($c_{238}[0]$ and $c_{230}[0]$) or ^{232}Th concentrations ($c_{232}[0]$) according to the zonal patterns represented by Figure 8a. The diffusion equations were numerically integrated adopting a Crank-Nicholson scheme in combination with an alternating-direction implicit method for solving the 3-D case (Press et al., 1992). The diffusant concentration in the external environment was held at zero. Mean concentrations of ^{206}Pb and ^{208}Pb were then obtained for each crystal zone by integration of the diffusion results. The zone results are displayed in terms of ^{206}Pb/^{238}U and ^{208}Pb/^{232}Th ages in Figure 8b.

It was found that variable time steps Δt satisfying the condition

$$\Delta t \leq \frac{(\Delta w)^2}{2 \cdot D(t)} \text{ (Press et al., 1992, p. 847).} \tag{A5}$$

where Δw equals the spacing of the diffusion cells (equal widths used in x, y and z directions), were producing precise results. Refinement of Δt values by a factor of ~4 (30,625 instead of 7959 steps total) resulted in negligible changes of final zone concentrations (e.g., ≤12 ppm for ^{206}Pb). Refining the grid by division into 121 × 481 × 241 grid points (14,026,411 instead of 4,186,161 grid points total) changed zone concentrations by ≤0.1%, indicating that the numerical results are robust.